

REPORT DOCUMENTATION PAGE

*Form Approved
OMB No. 0704-0188*

The public reporting burden for this collection of information is estimated to average 1 hour per response, including the time for reviewing instructions, searching existing data sources, gathering and maintaining the data needed, and completing and reviewing the collection of information. Send comments regarding this burden estimate or any other aspect of this collection of information, including suggestions for reducing the burden, to Department of Defense, Washington Headquarters Services, Directorate for Information Operations and Reports (0704-0188), 1215 Jefferson Davis Highway, Suite 1204, Arlington, VA 22202-4302. Respondents should be aware that notwithstanding any other provision of law, no person shall be subject to any penalty for failing to comply with a collection of information if it does not display a currently valid OMB control number.

PLEASE DO NOT RETURN YOUR FORM TO THE ABOVE ADDRESS.

1. REPORT DATE (DD-MM-YYYY) 10-03-2012		2. REPORT TYPE Final		3. DATES COVERED (From - To) March 2009 - December 2011	
4. TITLE AND SUBTITLE Robotic navigation emulating human performance: research plan.				5a. CONTRACT NUMBER	
				5b. GRANT NUMBER FA9550-09-1-0207	
				5c. PROGRAM ELEMENT NUMBER	
6. AUTHOR(S) Zygmunt Pizlo, Longin Jan Latecki				5d. PROJECT NUMBER	
				5e. TASK NUMBER	
				5f. WORK UNIT NUMBER	
7. PERFORMING ORGANIZATION NAME(S) AND ADDRESS(ES) Purdue University, West Lafayette, IN Temple University, Philadelphia, PA				8. PERFORMING ORGANIZATION REPORT NUMBER	
9. SPONSORING/MONITORING AGENCY NAME(S) AND ADDRESS(ES) AFOSR, 875 N. Randolph Street, Arlington VA				10. SPONSOR/MONITOR'S ACRONYM(S) USAF; AFOSR	
				11. SPONSOR/MONITOR'S REPORT NUMBER(S) AFRL-OSR-VA-TR-2012-0724	
12. DISTRIBUTION/AVAILABILITY STATEMENT Public Available Unlimited					
13. SUPPLEMENTARY NOTES					
14. ABSTRACT We formulated a set of computational tools (models) that allow a robot to "see" a natural 3D scene and to "understand" it in the sense that it can recover the 3D shapes, sizes and locations of the objects in the scene as well as the free spaces among them. The Figure-Ground Organization and 3D shape recovery tools built into our robot permits it to perform both of these complicated tasks on its own. In other words, all of the major steps required for 3D shape and scene recovery have been accomplished and they can be performed autonomously by a robot at this time. The remaining steps are designed to enhance its performance, bringing it in line with the performance of human beings. Once they are accomplished, our robot will not only be able to act autonomously; it will also be able to navigate within natural scenes as well as a human being can navigate under similar conditions. There is even good reason to believe that the FGO and 3D shape-recovery tools that you have seen work so well for our robot are actually rather similar to those used by human beings performing similar tasks. We tested these tools in human psychophysical experiments and showed that the human and the model's performances were very similar. Even if we ignore this psychophysical support, the mere fact that the					
15. SUBJECT TERMS					
16. SECURITY CLASSIFICATION OF:			17. LIMITATION OF ABSTRACT	18. NUMBER OF PAGES	19a. NAME OF RESPONSIBLE PERSON Zygmunt Pizlo
a. REPORT	b. ABSTRACT	c. THIS PAGE			19b. TELEPHONE NUMBER (Include area code) 317 796 5225

Reset

Robot navigation emulating human performance

Introduction

The basic idea underlying our new approach for recovering natural 3D scenes makes use of mechanisms employed by human beings to recover 3D shapes from 2D images (Li et al., 2009; Pizlo, 2008; Sawada & Pizlo, 2008; Li, 2009; Sawada, 2010; Pizlo et al., 2010). The novel, critical aspect of our approach is that *a priori* constraints are at least as important in 3D vision as visual data. This approach is different from all other, more conventional approaches in which the reconstruction of 3D shapes and 3D scenes is a hierarchical process based on a number of independent visual modules responsible for acquiring and combining pieces of visual information, called “depth cues”, e.g., texture, shading, motion, disparity, and vergence. Our novel approach, described with David Marr’s (1982) widely-known terminology, bypasses a viewer-centered representation by recovering geometrical properties of objects and their environment in an object-centered representation. Our approach is preferable to the conventional approach for two different, but related reasons. First, it is known that despite the fact that the human beings’ perception of 3D distances and 3D sizes is usually *not* veridical, the human being’s perception of 3D shapes *is always* veridical.¹ Second, several very effective *a priori* constraints for the perception of 3D shape are known, but no effective constraints are known for the perception of the 3D distances between pairs of 3D points. An additional advantage inheres in starting to recover 3D scenes with 3D shapes. Starting with 3D shapes allows the observer to “see” the “invisible” back parts of opaque objects. Paraphrasing Bartlett (1932) to put our novel approach into a broad historical perspective, we can say that using 3D shapes to construct 3D scenes allows an observer to actually “go beyond the information given”. The special role and significance of shape in visual perception was appreciated and highlighted by the Gestalt Psychologists almost a 100 years ago, but the mathematical and computational tools necessary to formulate their ideas and to make use of them in computational models did not become available until recently. This report reviews several of these tools and illustrates how they can be applied to the recovery of a natural 3D scene, like the scene shown in Figure 1.

We started working on this project because we believe that, at present, the best way to test any theory in vision is to implement a computational model of the underlying perceptual mechanisms and to show that it can be used effectively by an autonomous robotic system. This kind of robotic system acquires visual information, and then plans and executes actions without any intervention by the designer of the system. We have succeeded in developing a computational model that does this. It recovers a 3D object from one of its 2D images and then uses these mechanisms to recover naturalistic 3D scenes. These

¹By “veridical” we mean that the percept of the shape of an object agrees with its shape in the real world. Note that we are ignoring laboratory experiments that were designed specifically to demonstrate the failure of shape veridicality by using degenerate shapes and/or degenerate viewing directions.

scenes permit the robot to perform complex navigations without any aid from a human being, the kind of activity previously only performed by an alert, human being.



Figure 1. Five man-made 3D objects within a natural scene (the room used for robot navigation). A camera mounted on the top of this robot provides the visual information used to guide its navigations. An inclinometer, mounted on top of the camera, provides the robot with the information it uses about the direction of gravity.

Note that ours is not the approach most often used by others working in vision today. Vision researchers, more often than not, simply state what they call a “theory” in plain English and go on to describe some qualitative aspects of what they believe to be a potential perceptual mechanism. Even when a contemporary vision researcher has actually used a mathematical or computational model, more often than not, it was tested with synthetic images or only with a few hand-picked real images. Such tentative and partial approaches to providing an explanation of a limited visual process was justifiable some years ago but we believe that we have reached the point at which vision researchers should be much more ambitious. A nearly complete, working theory of at least some particularly significant aspect of visual processing should be provided now that this is no longer beyond reach. Meeting such expectations can be best served by verifying that any current theory meets at least two criteria, namely, that: (i) it is relatively complete, and (ii) it has no implicit or unjustified explicit assumptions. The best way to do this is to build a machine that can actually see as we do, a more complex act than is commonly assumed.

Traditionally, the visual and the motor systems have been treated as separate, independent modules that could be and were studied separately. But the fact that they are not nearly independent and that they can, and should be, studied as they work together, rather than separately, was emphasized by Dewey (1896) more than 100 years ago. He emphasized that perception is not, and should not be treated as, a passive process. Perception is only one part of a closed, continuously active “reflex arc”, actually more like a circle or a loop, called the “perception-action cycle”, in which perception and motor action follow one another and interact continuously in everyday life. This observation is not only very old, it was picked up, promulgated, mulled over and elaborated by many others since it was

proposed, most notably by Hebb (1949) and by Gibson (1966), who attempted to include this interaction in their “verbal models” of what is now often referred to as “ecologically-valid vision”. Note that the integration of vision and action, originally proposed by Dewey, who credits William James (1890) for pointing him in this direction, makes a lot of sense, despite its neglect in most contemporary work, for at least two reasons. First, an observer must actively seek information about the environment by using more than one viewing direction. The observer must do this to determine whether his initial viewing direction provided all of the information required to perceive the scene veridically. Second, the observer needs veridical information about the environment because it is essential for the efficient planning and successful execution of the specific behavioral acts that will achieve the desired goals. The reader will surely agree that the best, perhaps even the only, way to study such complex, but very natural, interactive processing is to develop a model that sees and acts, as the human being does, and furthermore, that this model should be realized in the form of a mobile robot now that they are available “off-the-shelf.” Note that this approach is not novel. It was first proposed long before its implementation was viewed as either possible or imminent. It goes back at least to Richard Feynman, who is reported as having said “what I cannot create I don’t understand” and/or was proposed at the early stages of cognitive science by Miller, Galanter & Pribram (1960) who said that “The creation of a model is proof of the clarity of the vision. If you understand how a thing works well enough to build your own, then your understanding must be nearly perfect (p. 46).” So, all we are really saying here, is that it is time to put these words into practice.

This final report begins with a description of why, as well as how, a camera should be calibrated when it is used for “machine vision”. This is followed by a description of the most important features of our 3D shape recovery model. These features will be presented with special emphasis on the nature and role of our model’s *a priori* constraints. Next, problems inherent in the recovery of the shape of a 3D scene are stated and possible methods of solving these problems are described. The solutions call attention to the importance of non-visual, as well as to visual, *a priori* constraints. Note that by recovering the shape of a 3D scene, we mean recovering the geometry of the 3D scene up to one unknown parameter, namely, the overall scale of the scene and the objects within it. The scale can be based on the estimation of a *single* distance in a 3D scene. The height of the observer, a human or a robot, can serve as a particularly useful single distance for a potential navigator. Finally, having explained what it takes to recover 3D shapes and then to use this information to recover a 3D scene, we will describe the first step in visual processing, which is usually referred to as Figure-Ground Organization (FGO), the terminology favored by the Gestalt psychologists a century ago. Discussing FGO, the very first stage of visual processing last, will allow us to actually specify what the output of the first stage of visual processing should be like. Prior to our new approach to the recovery of 3D shapes and 3D scenes, there was not even a good definition of what Figure-Ground Organization was, much less of what Figure-Ground Organization should accomplish or how this could be done.

In our approach, FGO refers to (i) finding the 2D region and its occluding contour for each object in the 2D image, as well as to (ii) finding the 3D region and its bounding box

in the 3D scene “out there”, where the object resides. Once this is done, the internal contours required for 3D shape recovery are extracted and the 2D information about the 3D symmetry of the shape and the planarity of its contours are determined and included in the description of the “figure” by labeling its contours. It is clear that in our approach, FGO refers both to properties of the 2D image and to properties of the 3D shape. This differs from the conventional view of FGO that limits FGO to 2D features. Note that our claim that FGO includes 3D, as well as 2D features, was suggested by the Gestalt Psychologists when they emphasized that the organized figure is always perceived in front of its background, which is perceived as lying behind as well as around the figure.

1. Calibration of the camera

The order of the next sections does not reflect the order of the computations by the visual system or the order of importance of our computations. The order simply reflects what we believe to be the best and simplest way of explaining what we did and why we did it. Why it is important to calibrate your camera if you want to use it in research on visual perception will be explained below. We start with the definition of a “camera matrix”. Most of the equations presented in this paper use this matrix. The process of estimating a camera’s matrix is called “camera calibration”. A camera matrix is a 3 by 4 matrix that defines the geometric properties of a camera, like its focal length, principal point, etc. These properties characterize the perspective projection from a 3D scene to a 2D image. Why is the camera matrix important? Consider a psychophysical experiment on the perception of objects from perspective images, such as photographs. The geometrical properties of these photographs must be known if the experimenter wants to show photographs of the objects to his subject. Specifically, the subject’s eye (more precisely, the center of the perspective projection of the eye, called its “nodal point”) must be placed at the center of the perspective projection for any given picture. This must be done if you want the retinal image in the subject’s eye produced by the *perspective* photograph of the 3D object to be a *perspective* image of the 3D object. This is how the first demonstration of the rules of perspective projection was done almost 600 years ago by Brunelleschi (see Kubovy, 1986). This method is still used by modern students of vision to set up their experiments, *e.g.*, Attneave & Frost (1969). If the eye is placed at any other point than at the center of the perspective projection, the retinal image produced by a perspective photograph of a 3D object will not be a valid perspective image of this object. Instead, it will be an image of a 3D *projective* transformation of the object because a perspective picture of a perspective picture is not, itself, a perspective picture (Pizlo, 2008). Failing to use a *perspective* projection will almost always lead to a non-veridical percept of the 3D object (see Pirenne, 1970; Kubovy, 1986; for examples of such distortions). The bottom line is that ***when 2D perspective images are used for making 3D inferences, the parameters of the camera that took the images must be known.***

Now that you appreciate why a camera matrix is important, we will describe it in detail. Consider the relation between a 3D point V^* in front of a camera and expressed by homogeneous coordinates $(V_X^*, V_Y^*, V_Z^*, V_W^*)^T$ and its 2D camera image v^* also expressed by homogenous coordinates $(v_x^*, v_y^*, v_w^*)^T$. Equation (1) represents the perspective transformation from V^* to v^* :

$$v^* = KQV^* \quad (1)$$

Where

$$K = \begin{pmatrix} \alpha_x & s & u_0 \\ 0 & \alpha_y & v_0 \\ 0 & 0 & 1 \end{pmatrix} \text{ and } Q = (R_{3 \times 3} \quad -R_{3 \times 3}C_{3 \times 1})$$

Matrix K is called the “intrinsic matrix”. It defines the camera’s intrinsic properties, such as its focal length. Matrix Q is called the “extrinsic matrix”. It represents the transformation from the world coordinate system to the camera coordinate system. This transformation consists of a 3D translation ($-C_{3 \times 1}$) followed by a 3D rotation ($R_{3 \times 3}$). The geometric details of R and C are described in the following paragraphs. The product of the intrinsic matrix (K) and the extrinsic matrix (Q) is called the “camera matrix” (P)

$$P = KQ \quad (2)$$

In equation (1), the 3D point and its image are expressed by homogeneous coordinates because they allow expressing a non-linear perspective projection by using matrix notation. The transformation between the Euclidean coordinates and the homogenous coordinates for a 3D point $(V_x, V_y, V_z)^T$ and a 2D point $(v_x, v_y)^T$ is expressed as follows:

$$(V_x \quad V_y \quad V_z)^T = (v_x^* \quad v_y^* \quad v_z^*)^T / V_w^* \quad (3a)$$

$$(v_x \quad v_y)^T = (v_x^* \quad v_y^*)^T / v_w^* \quad (3b)$$

assuming that V_w^* and v_w^* are not equal to zero.² The equations (3a) and (3b) imply that the homogenous coordinates of a point are not unique. For example, $(1, 2, 3, 1)^T$ and $(2, 4, 6, 2)^T$ represent the same 3D point. In practical applications, V_w^* can usually be set to 1. This way, 3D homogenous coordinates are trivially obtained from 3D Euclidean coordinates (and vice versa). The representation of a 3D plane in homogenous coordinates is the same as that of a 3D point: both are four-element vectors. For example, if π^* is a 3D plane, then all points V^* on π^* satisfy $\pi^{*T}V^*=0$. Similarly, in a 2D image, the representation of points and lines in homogenous coordinates are the same, and they are three-element vectors.

In this report, some equations use both homogenous and Euclidean coordinates. To avoid confusion, symbols *with asterisks* represent the homogenous coordinates of geometric primitives, like points, lines, or planes. The symbols *without asterisks* represent the Euclidean coordinates. The individual parameters in the camera matrix are described next.

² In homogenous coordinates, if the last value of a vector is equal to zero, the vector represents a point at infinity.

Consider the parameters in the intrinsic camera matrix (K). $(\mu_0, \nu_0)^T$ is the principal point of a camera, the point of intersection of the camera image plane with a line emanating from the center of a perspective projection that is orthogonal to this plane (see Figure 3). The principal point is close to the center of the camera image, but it is never exactly at the center, due to technical limitations inhering in the design of the camera. Why are there such limitations? Consider the fact that when the physical size of a camera's image, containing 2000 by 3000 pixels, is less than one centimeter, the displacement of the center of the camera lens by as little as one millimeter translates into a displacement of the principal point by more than 100 pixels. This makes it almost impossible to mount the lens exactly in front of the center of the camera's image. The green dot in Figure 4 represents the center of the picture and the white dot represents the principal point of the camera that was used to make most of the examples included in this paper. In our setup, this point is displaced from the center of the image by about 0.6 degree. This amount of error in estimating image points would have dramatic implications for binocular (stereoscopic) analysis of the 3D space. In the human eye, the principal point corresponds to a region of best vision near the center of the retina, called the "fovea". The fovea is well-defined both anatomically and perceptually. Anatomically, the flat floor of the fovea is a disc with a diameter of about 1.5 degrees. It contains only receptors, called "cones". Perceptually, the fovea serves as the center of the visual field. It is the region in which detail vision is most acute. When an observer orients his eye to look directly at a feature in order to examine its details, the eye's orientation will cause the feature's retinal image to fall at the center of the fovea, where it is said to be "fixated". An observer can maintain fixation of an attended object with high precision: the standard deviation of eye position during maintained fixation is only 3 or 4 minutes of arc (Steinman, 1965). This is equivalent to only two pixels in a camera whose field of view is 60 degrees and whose image is an array of 2000 by 3000 pixels.

The next intrinsic camera parameter considered is called its "focal distance". The focal distance is the distance between the center of a perspective projection and the camera image (Figure 3b). In the intrinsic camera matrix, the focal distance is defined in terms of the number of pixels along the X axis (α_x) and Y axis (α_y) in the camera coordinate system. In other words, both the interval of length α_x pixels along the X axis and the interval of length α_y pixels along the Y axis are equal to the focal length. In modern cameras, the difference between α_x and α_y is very small, so we can assume that they are equal. In the human eye, the focal distance is about 2cm, which is the approximate diameter of the human eyeball. The third intrinsic parameter of a camera is called the "skew" (s) which specifies how much a pixel is biased from a perfect rectangle. For most modern cameras, the skew parameter is zero.

There is one more intrinsic camera parameter. It measures what is called its "radial distortion". This parameter is not expressed in Equation 1 because the radial distortion cannot be represented as a linear transformation. In an image with radial distortion, the straight lines at the periphery tend to be curved (see Figure 2). Radial distortion is obvious with cameras that have a large field of view (e.g., 60 deg) or a small focal length.

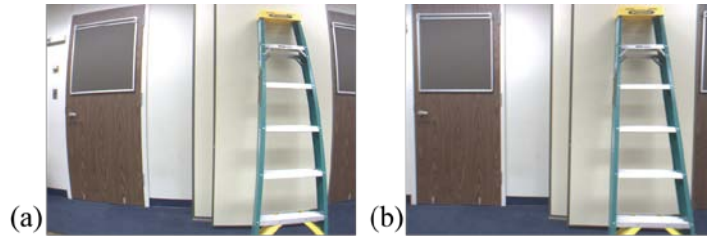


Figure 2. (a) Radial distortion of a wide angle camera. (b) the image from (a) after calibration.

Now consider the extrinsic matrix Q . It defines the transformation between the world coordinate system and the camera coordinate system. The specification of the world coordinate system depends on the application. For example, if the task is to recover a 3D scene in a room, it is natural to use one of the corners of the room as the origin and the three edges of the room emanating from this corner as the X, Y and Z axes. The camera coordinate system does not actually depend on the application. It is a fixed characteristic of the camera. This coordinate system is defined as follows: the origin is the center of perspective projection of the camera. The XY-plane is parallel to the camera image plane. The X axis coincides with the X axis of the camera image. The Z axis represents the depth direction (see Figure 3a). The vector C in Q is the projection center expressed in the world coordinates. $R_{3 \times 3}$, a rotation matrix, represents the orientation of the camera coordinate system. Specifically, the three row vectors in R correspond to the directions of the X, Y and Z axes of the camera coordinate system expressed in the world coordinate system.

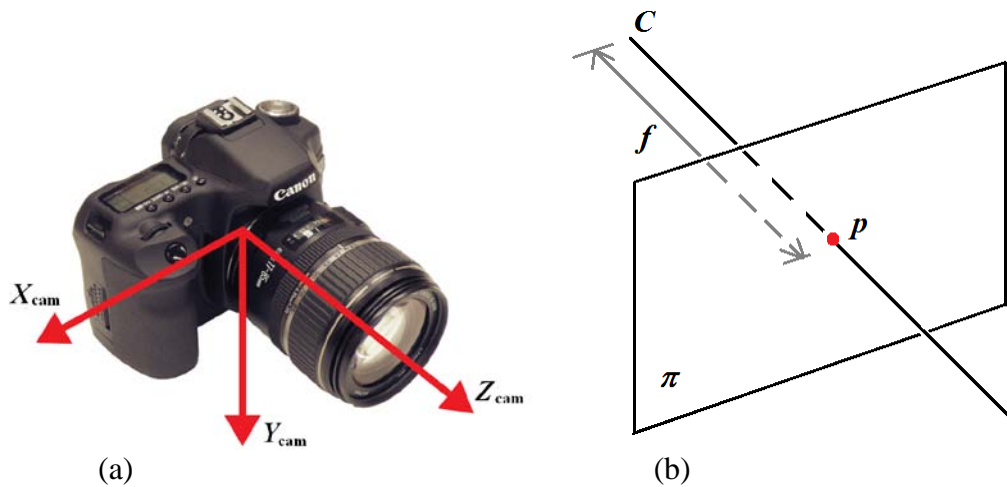


Figure 3. (a) The camera's coordinate system. (b) Schematic illustration of a camera. C represents the projection center. p is the principal point. The line pC is orthogonal to the image plane π . f represents the camera's focal length.

It follows that the camera matrix not only includes a camera's properties, but also its orientation and position in an environment (see Faugeras, 2001, and Hartley & Zisserman, 2003, for more details of the camera matrix). The process of estimating camera

parameters is called “camera calibration”. A camera is calibrated by acquiring multiple images of a reference scene, whose geometry is known. Once the 3D coordinates of the scene and the 2D coordinates in its image are known, one can solve for the camera’s unknown intrinsic and extrinsic parameters. Open access software for calibrating a camera, can be found at (e.g., OpenCV: <http://opencv.willowgarage.com/wiki/FullOpenCVWiki>).

2. Recovery of a 3D shape and a 3D scene

The camera matrix defines a camera’s geometry – it specifies how to project a 3D point onto a 2D image plane. Given a 3D point, its image is uniquely determined. Therefore, generating a 2D image from a 3D scene is an easy “forward problem” (Poggio et al., 1985; Pizlo, 2001). However, the “inverse problem”, recovering a 3D scene from its 2D image, is difficult because the solution is not unique, i.e., for any given 2D image point, there are infinitely many 3D points that can produce the same 2D image point. Inverse problems are almost always difficult because they are “ill-posed” and “ill-conditioned”. In plain English, inverse problems are “insoluble”. The only way to solve an inverse problem is to impose *a priori* constraints on the family of possible interpretations, and then combine these constraints with the available data to find the most reasonable solution. Ideally, it will be the correct, veridical, interpretation of the conditions in the physical world.

The *symmetry* of the 3D shape is a strong *a priori* constraint. Given a 2D perspective image of a symmetrical 3D shape, its symmetrical 3D interpretation is unique except for the size and position. The following equations show how to use the camera matrix (P) to recover a pair of 3D symmetric points (X_1 and X_2) from their 2D image (x_1 and x_2) if the vanishing point v for the line connecting X_1 and X_2 is given.³

The camera matrix P is a 3 by 4 matrix. It can be decomposed and expressed as follows

$$P = (M_{3 \times 3} \quad p_4) \quad (4)$$

M is a 3 by 3 matrix that consists of the first three column vectors of P and it is equal to the product of the intrinsic matrix (K) and the rotation matrix (R). p_4 is the fourth column vector of P . Let x_1 and x_2 be expressed by the Euclidean coordinates and x_1^* and x_2^* be their homogenous coordinates with the third element equal to 1. Then the set of all 3D points whose image is x_1 (or x_2) can be expressed as follows (eq. 6.14 in Hartley & Zisserman, 2003):

$$X_i = M^{-1}(k_i x_i^* - p_4) \quad i = 1, 2 \quad (5)$$

³ The vanishing point in the image is the intersection of the lines connecting the images of pairs of 3D symmetrical points. In 3D space, all of these lines are parallel to one another. In a perspective image, they all intersect at the vanishing point.

k_i are free parameters. For the solutions X_1 and X_2 to be symmetrical, k_1 and k_2 must satisfy the following equation (refer to Appendix A for the derivation).

$$\begin{pmatrix} v^{*T} M^{-T} M^{-1} x_1^* & v^{*T} M^{-T} M^{-1} x_2^* \\ |x_1 - v| & -|x_2 - v| \end{pmatrix} \begin{pmatrix} k_1 \\ k_2 \end{pmatrix} = \begin{pmatrix} 2v^{*T} M^{-T} M^{-1} p_4 - 2d \\ 0 \end{pmatrix} \quad (6)$$

For the recovered pairs of symmetrical 3D points, the normal of the symmetry plane is determined by the vanishing point v , and is equal to $M^{-1}v^*$. The position of the symmetry plane is determined by the parameter d . d is a free parameter and it can be any real number, which determines the size (or position) of a recovered 3D object. Figure 6a shows five objects recovered from the same 2D camera image. Their symmetry planes have the same orientation, but different positions. The recovered object is small when it is close to the camera (the cyan box in Figure 6a). The recovered object is large when it is far from the camera.

Although equation (6) looks complex, it can be simplified in applications after making some assumptions about the camera's parameters. For example, if the skew s is equal to 0, α_x and α_y are identical, and the origin of an image coincides with the principal point, then K is a diagonal matrix ($K = \text{diag}(\alpha_x, \alpha_y, I)$). Furthermore, if the world coordinate system coincides with the camera coordinate system, then R is an identity matrix and p_4 is a zero vector. It follows that $M = K$.

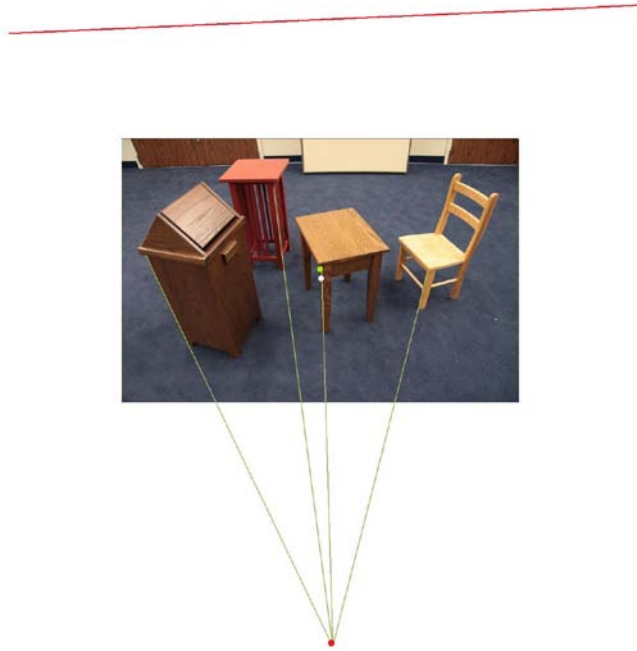


Figure 4. The red line above the picture of a 3D scene shows the horizon in this scene. The red dot below the picture shows the vanishing point corresponding to the 3D vertical lines. The principal point is marked by a white dot near the center of the image. The geometrical center of the image is marked by the green dot.

Equation 6 suggests that in order to recover a symmetrical 3D shape, the visual system needs to: (1) know where the vanishing point is and (2) establish which points in a 2D image, are the images of pairs of 3D symmetrical points. In order to accomplish these two things, two additional *a priori* constraints will be required, namely, the direction of gravity and a line representing the horizon.⁴

Computation of the vanishing point and identification of symmetric pairs

Gravity is the most critical constraint operating in our environment. Gravity is not only responsible for stability in our environment, it is also most likely to be responsible for the symmetry of almost all animals' bodies. If the ground plane is horizontal, it is orthogonal to the direction of gravity. An animal's body will be stable if its body is symmetrical with respect to the plane parallel to the direction of gravity. A symmetrical animal will not fall on its side when it stands. It follows that given a symmetrical 3D shape standing on a horizontal ground, the line segments connecting the symmetrical points are parallel and orthogonal to gravity. For all parallel lines that are orthogonal to gravity, their vanishing points fall on a horizon. If the ground plane is not horizontal, the symmetry line segments of symmetrical objects standing on the ground are parallel to the ground but not orthogonal to the direction of gravity. The corresponding vanishing line is then determined by the actual ground plane, not by the plane orthogonal to the direction of gravity.

Assume that the normal of the ground floor is N_h in the world coordinate system, then the horizon (i.e., the vanishing line corresponding to the horizontal ground plane) is expressed as follows (Result 8.16 in Hartley & Zisserman, 2003):

$$l_h^* = M^{-T} N_h \tag{7}$$

For a calibrated camera, the horizon is known *before* the image is taken, which means that this information is truly *a priori*. Once the horizon is known, we can search for the vanishing point, which is the intersection of the 2D symmetry line segments of a given object. Since the vanishing point must be on the horizon, the search is determined by only one free parameter. Without the horizon, there are two unknown parameters specifying the position of the vanishing point, and the point cannot be estimated reliably (specifically, its distance from the object's image in the 2D camera image). The horizon provides a very strong constraint for this less reliable parameter. Equation (7) shows that the horizon is equal to the product of the direction of gravity and the inverse of transposed M . Because M (the product of the intrinsic matrix K and the rotation matrix R) is unrelated to the position of the camera (C), the translation of the camera in 3D space leaves the horizon and all vanishing points in the image invariant. These invariant features are likely to be useful in robot navigation.

⁴ The horizon is a vanishing line on the image plane, which is a perspective projection of the line at infinity on any plane parallel to the horizontal ground plane.

The vanishing point on the horizon is obtained by computing the intersection between the symmetry lines (the green lines in Figure 5b) and the horizon (the blue line). The green lines (contours in the image) are not always perfectly straight. Therefore, the first step in computing the vanishing point is to approximate (by using least squares) the symmetry lines with straight lines.

Let x_i^* represent the 2D points on a symmetry line. Let $A_{k \times 3} = (x_1^* \ x_2^* \ \dots \ x_k^*)^T$. Then the approximating line l^* is parallel to the eigenvector of $(A^T A)_{3 \times 3}$ whose corresponding eigenvalue is the smallest⁵. Once each symmetry line is approximated by a straight line, we can estimate the vanishing point for these symmetry lines. Suppose for one object, $l_1^*, l_2^* \dots, l_n^*$ are the n symmetry lines. Because of noise, the intersections of symmetry lines with the horizon are not identical. Therefore, we estimate the vanishing point as the point that has the least square distance to all symmetry lines.

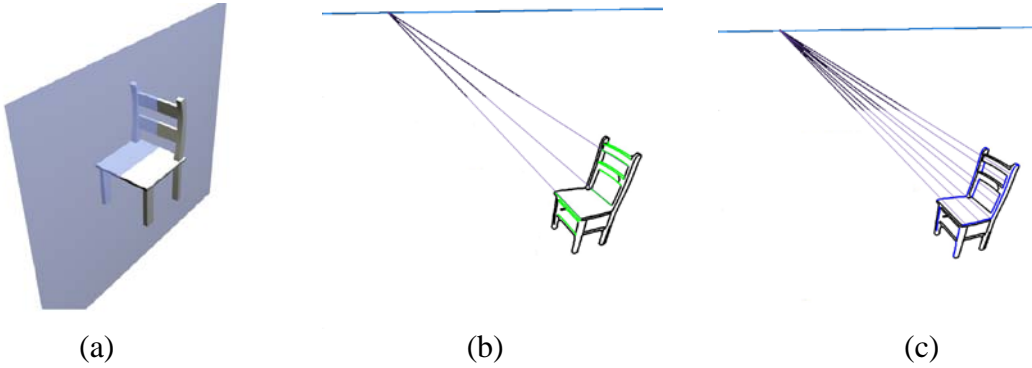


Figure 5. (a) The symmetry plane of a 3D object resting on the ground is vertical. (b) Symmetry lines segments are indicated by green. (c) Pairs of symmetrical contours are marked by blue.

Let the horizon $l_h^* = ((l_h^*)_x \ (l_h^*)_y \ (l_h^*)_w)$, then $m_h^* = (-(l_h^*)_y \ (l_h^*)_x \ 0)$ represents the direction of the l_h^* . Suppose v_0^* is one point on the horizon such that $(v_0^*)^T l_h^* = 0$, then the vanishing point is estimated as:

$$v^* = v_0^* + u m_h^* \quad (8)$$

⁵ The singular value decomposition (SVD) method can be used to find eigenvectors. The matrix A can be decomposed and expressed as $A = USV^T$ where U and V are orthonormal matrices. S is a diagonal matrix and its values are sorted in a descending order. The direction of the approximating line is represented by the last column vector of V .

where $u = -\frac{(m_h^*)^T B^T B v_0^*}{(m_h^*)^T B^T B m_h^*}$ and $B = (l_1^* \quad l_2^* \quad \dots \quad l_k^*)^T$. The derivation is given in

Appendix B.

Once the vanishing point is estimated, the pairs of points in the 2D image, which are images of symmetrical points of an object can be established as intersections of pairs of corresponding contours and the lines emanating from the vanishing point (see Figure 5c). The 3D symmetrical shape can then be recovered by recovering all pairs of symmetrical points according to equation (5).

Recovery of the hidden part

We just showed how to recover pairs of symmetrical 3D points by using equation 5. Note, however, that in order to recover a 3D point, both the image of this point and of its symmetrical counterpart had to be known. In other words, the symmetrical pairs in a 2D image must be visible. For example, the back, the seat and the front legs of the chair in Figure 5b can be recovered on the basis of the symmetry constraint because their corresponding symmetrical contours are visible. However, the two rear legs cannot be recovered by using symmetry alone because one of the legs is hidden. In this case, we begin by using the planarity constraint to recover the point of the chair that is visible. The contours representing the right side of the chair shown in Figure 5b are coplanar (approximately) and we can estimate the plane containing these contours from the points and contours that were recovered by using equation 5 (they could be recovered because both symmetrical pairs were visible). Once this is done, the intersection of this plane and the plane defined by the image of the visible right rear leg and the projection center of the camera, is a 3D line containing the recovered right rear leg. Its invisible, symmetrical counterpart is obtained by reflecting the recovered right rear leg with respect to the symmetry plane (see Li, Pizlo & Steinman 2009 for details).

Recovering the shape and scale of a natural 3D scene

We pointed out (above) that for the recovered 3D shapes, their sizes and their positions are undetermined, but “placing” them on the ground will make it possible to uniquely determine the relative positions, sizes and pair-wise distances among all of the 3D objects. When the shape of a 3D object is recovered, the object can either be small and close to the camera, or large and far from the camera (see Figure 6a). Once the height of a camera above the floor is known, there is ***only one*** size and ***only one*** corresponding distance at which a given object will be resting on the floor. For smaller distances, a recovered object would be floating in the air, and for larger distances, the object will be below the floor. Thus, regardless of the number of objects in the scene, their sizes, positions and distances are determined by only one parameter, namely the height of the camera. Ambiguity only remains for objects whose relative position with respect to the floor is unknown: this occurs whenever the bottom part of an object is occluded. Whenever this happens, the size and distance of the object will be uncertain. But, because real objects cannot occupy the same physical space, this uncertainty can be reduced by using information obtained from nearby objects. Figure 6b shows the recovered 3D scene for the picture in Figure 4.

The online demo at <http://web.ics.purdue.edu/~li135/SceneRecover.html> shows an animation of this recovery. The widths and heights of the children's chairs were about 30 cm. The accuracy of our size and distance recovery can be evaluated by comparing their distances and sizes to the 20 cm. wide unit-square scale shown on the floor. The position and the orientation of the robot's camera used to make this image are indicated by the cyan box. These results show that our algorithm not only recovered the size and distance of the 3D objects accurately, it recovered the entire objects, including their invisible back contours!

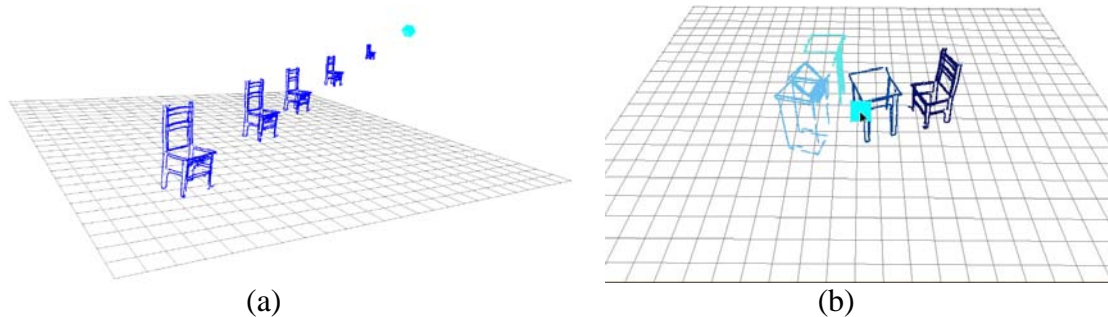


Figure 6. (a) Recovering the size and position of a 3D object. The small green cube represents the 3D position of the robot's camera. (b) The image of a recovered 3D scene (for on-line demo go to: <http://web.ics.purdue.edu/~li135/SceneRecover.html>)

The methods described in this section are illustrated by providing the reader with an on line Matlab program and data (<http://web.ics.purdue.edu/~li135/JMP2011/JMPDemo.rar>). The image shown in Figure 4 is the image used for the 3D recovery. The 2D contours extracted from this image is the input data. The Matlab program will perform the 3D recovery of the contours as described in this section. The reader is encouraged to use the program to recover the 3D scene represented in Figure 4, and also to use this program with their own images after their camera has been calibrated (see above).

3. Figure-Ground Organization (FGO)

In the Introduction, we enumerated the tasks that had to be accomplished when we want to recover a 3D scene. One of these tasks, isolating objects from their background, was called the Figure-Ground Organization (FGO) problem. The fundamental importance of this problem was pointed out by the Gestalt Psychologists almost 100 years ago, but they made very little progress in developing it primarily because they lacked the mathematical and computational tools to do so. Following the Cognitive Revolution, such tools became available: computers were built, Information Theory was formulated, and Cybernetics was established as an interdisciplinary specialty to integrate engineering, biology and psychology. Unfortunately, the progress made in the development of applied mathematics, computer science and electrical engineering did not include any important advances in our understanding of the most important basic problem in vision, *viz.*, the FGO problem that our machine had to solve. This absence of significant progress with the FGO problem

allowed the vision community to stop worrying about how important it was and, in time, they even began to denigrate this as well as many other contributions of the Gestalt Psychologists to visual perception. The few who did try to work on it tried to formulate theories and models of FGO without clarifying the ill-defined concepts used by Gestalt Psychologists before the Cognitive Revolution. This led to a lot of confusion in the machine vision community on one side and in the human vision community, on the other. This confusion would (and should) have been avoided if “visionists” on both sides had remembered the question that actually underlay the FGO problem, namely, how does the human observer see real 3D objects in natural 3D scenes veridically on the basis of the information provided by 2D real retinal images. Human beings, as well as other animals, obviously do. How do they do it? Ignoring, or downplaying the importance of studying real viewing conditions inevitably changed the nature of the problem. Confining efforts to the study of 2D stimuli should not, and did not, lead anywhere.

Finding objects in the 2D image and in the 3D scene

We begin by considering how the traditional approach tries to distinguish objects from their backgrounds. This approach uses information only present in a pair of 2D images with slightly different views of the scene. The pair can be obtained either by using two eyes (“binocular disparity”) or by using successive images from a single eye (“motion parallax”). Julesz (1971) provided strong support for the functional advantages inherent in having more than one view of a scene by showing that binocular disparity and motion parallax are critical in breaking camouflage. His most compelling support for this claim was obtained when he showed that perceptions of 3D spatial relations can be produced with “random-dot-stereograms”. Such stereograms contain no useful monocular information about the objects that are actually present in the visual field.

Figure 7 illustrates what can be accomplished by using two different images. The camera mounted on our robot acquired a pair of stereoscopic images that it used to detect and locate the 3D objects represented in its pair of 2D images (see Figure 1). The robot started the process by using binocular disparity to compute a 3D map. This was done by using an off-the-shelf algorithm for solving the stereo-correspondence problem (Wong, Vassiliadis & Cotofana, 2002). Two computational steps were then used by the robot to construct a top view of the 3D scene, specifically, the 3D points cloud was computed from stereo disparity by using the triangulation method, and the floor was approximated by finding a 3D plane which contained the maximal number of points. Note that this step was also used to calibrate our robot’s camera, namely, we computed the orientation of the robot’s camera and its position relative to the floor (see the parameters of the extrinsic matrix). The detection of the floor is an important step because:

- (1) one can remove the points close to the floor and beneath it once we know where it is;
- (2) one can project the remaining 3D points onto the floor to generate a top view image. The white dots in Figure 7b show the top view image after the floor points were removed. This made the layout of the objects in the scene very clear.

We then identified the number of objects, their positions and their orientations by fitting rectangles within the top view image. The 3D distances, sizes and aspect ratios may not be very accurate in this top view, but all 8 objects present in this scene were detected and located relative to each other quite well. This is evident in the 2D image of Fig. 7b. It is clear that even at this early stage of analysis, the robot has obtained considerable information about this 3D scene. The top view clearly has sufficient information for the robot to plan navigations among all of these 8 objects. The top view of the furniture arrangement shown in Fig. 7b also makes it clear that the critical first step of FGO has been solved for this rather complex furniture arrangement. The computation of the top view and its use in solving the FGO problem makes intuitive sense because a top view of objects in most natural scenes is not likely to have one object occluding another. Furniture stacked in a storeroom might be a relatively common exception. Occlusions are common in the original view shown in Figure 7a because far objects are likely to be occluded by near objects but this does not present a problem when the top view is used. Using a scene-centered, rather than a viewer-centered, representation early in processing proved to be essential for solving the FGO problem.

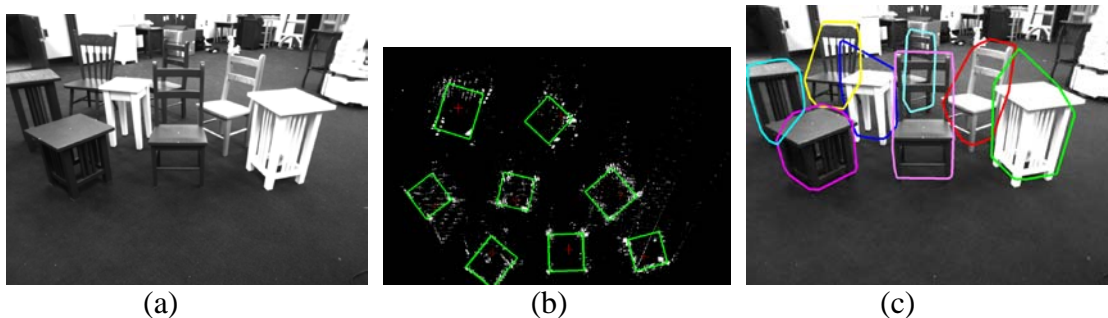


Figure 7. (a) A 2D image of a 3D scene containing children's furniture. (b) A top view of the 3D scene in (a) showing the 8 objects that were "seen" by the robot (the robot analyzed the 3D scene within a 3m viewing distance). The green rectangles represent individual objects, their sizes, aspect ratios and orientations. Note that even the occluded chair in the back of the scene was detected. The top view was produced from a pair of images acquired by the robot's stereoscopic camera. (c) The detected regions for individual objects in the 2D image.

If you want to do more than navigate in this environment, it probably will become useful to recover the actual 3D shapes of each of the 8 objects. Their 3D shapes will be the best way to identify them because their shapes will let you know their purpose, sitting on some and eating off others. Doing this requires obtaining 2D information about the edges representing each 3D shape. Detecting meaningful edges in a single 2D image is difficult because there are always many spurious edges in the image caused by texture and shading. The problem can be solved if the region in the image representing each individual object can be specified. Figure 7c illustrates how our model solved this problem. The model estimates the height of each object from the distribution of the 3D points that projected to a given rectangle in Figure 7b. This operation produced a 3D "bounding box" for each object. This 3D box is then projected to the original 2D image. This produces a convex region containing the image of the object. So, our method, as described in this section, can actually be used to produce both 3D and 2D FGO: it can also

be used to determine the spatial location of each of the objects on the floor as well as in the 2D image. Note that the 2-Dimensional FGO is based on a 3-Dimensional FGO. The 3D FGO is easier to perform so it is not surprising that it is best done before the 2D FGO. The 2D FGO is also critical, however, because it provides a means to transition from both the texture and surface information that were used to produce the depth map to the contours that are essential for recovering individual 3D shapes.

4. Extracting relevant edges

Now that we know that the recovery of 3D shapes depends entirely on contours, and that texture and surfaces play no role, we can ask how we can extract relevant (hence meaningful) contours of objects within a given scene? We need to know which contours belong to which object. Furthermore, we need to know how to organize the 2D contours in the retinal image so that this organization conveys sufficient information about the 3D shapes “out there” to permit an observer (human or robot) to function effectively in its environment. Considerable progress has been made in this direction recently. It is described in this and the next section.

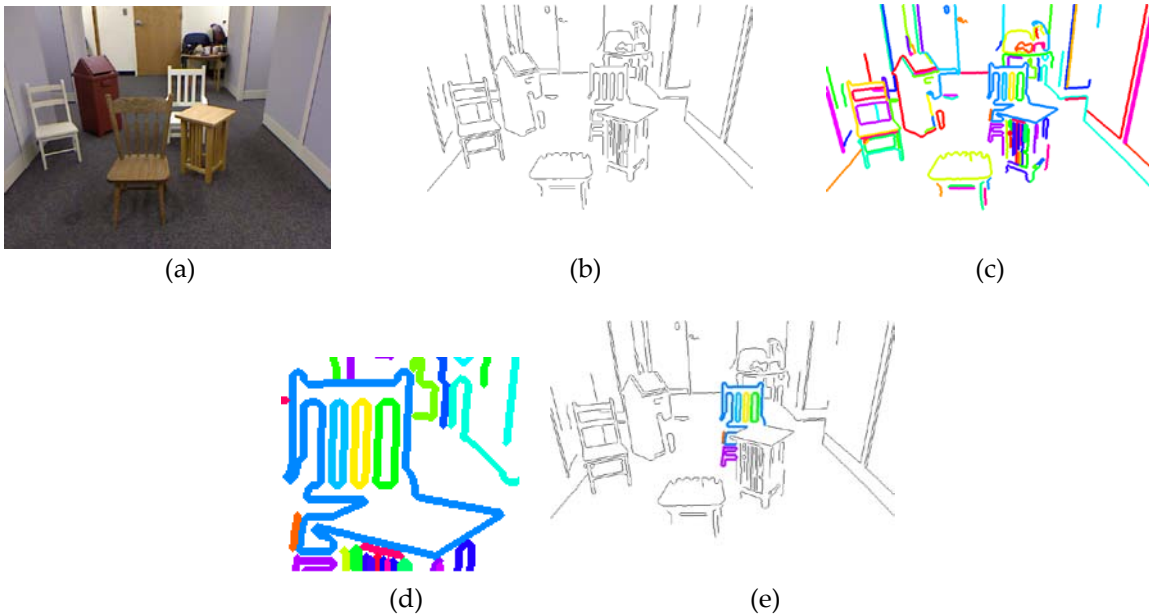


Figure 8. (a) An input image. (b) Its binary edge image. (c) These edges grouped to edge fragments. (d) Occluding contours of a foreground object *incorrectly* merged with the background objects. (e) Contours of a single object selected in the image when the FGO problem has been solved correctly.

The problem of extracting relevant (hence meaningful) edges in a 2D image that contains unfamiliar objects has traditionally been deemed to be an insoluble problem; a problem so difficult that many students of human and computer vision assume that a solution is actually impossible. The main difficulty traditionally seen arises from the fact that any edge-detection algorithm will detect at least 10 times as many edges as it should detect and will also miss some very important edges. These irrelevant (meaningless) edges are

produced in the image by such things as texture, occlusions, shadows and by specular reflections.

In computer vision, where most of the work has been done so far, the process of extracting relevant edges is called “contour grouping”. It begins by taking a color or a gray-level image (Fig. 8a) and reducing it to a binary image composed of edge pixels (Fig. 8b). The edge pixels are then grouped to form curves called “edge fragments”. Different edge fragments are shown in different colors in Fig. 8c. This is a greedy, low-level process. It uses only very simple processes such as proximity and good continuation and it uses them at the pixel level. Some other simple rules are often applied to eliminate edge fragments, *e.g.*, the removal of too short or wiggly fragments. These processes, however, are not likely to extract the true contours of 3D objects. An example of this kind of failure is shown in Figure 8d where contours of two different objects have been merged into a single contour. If such mistakes are not corrected, it will be impossible to perform a meaningful recovery of the 3D shape. The only algorithms developed to date that can produce correct results require familiarity with the 3D shape and its 2D images *before* the recovery can actually be made (Ferrari et al., 2006; Latecki et al., 2008; Yang & Latecki, 2010; Srinivasan et al., 2010; Toshev et al., 2010; Ma & Latecki, 2011; Andriluka et al., 2008; Lin et al., 2009). These algorithms assume that the observer saw multiple views of each object and stored them in memory. These stored views are then used to match the edges in the retinal or camera image. Clearly, this multiple-view theory is not only very cumbersome; it is actually implausible because the contours of the 2D image change in unpredictable ways whenever the viewing direction changes. To actually use this approach, one would need a very large number of 2D models for each 3D object. Considering that there is a huge number of possible objects in our environment, a large number of possible positions, as well as the large range of sizes of the objects in the 2D image, the matching problem inherent in this kind of algorithm leads to a combinatorial explosion.

We already knew that this problem can be solved easily without familiarity by human beings who see unfamiliar shapes veridically. Our robot can do it without familiarity, too. Furthermore, it can do it easily once the specific 2D region that contains the image of a specific 3D object has been determined (see Fig. 7c). With this known, the algorithm focuses its analysis on the small set of edge fragments that are located within this region. Concentrating the analysis on a meaningful, predefined 2D region substantially improves the likelihood of extracting the relevant set of contours because contours belonging to the background have been eliminated from consideration (see Figure 8e).

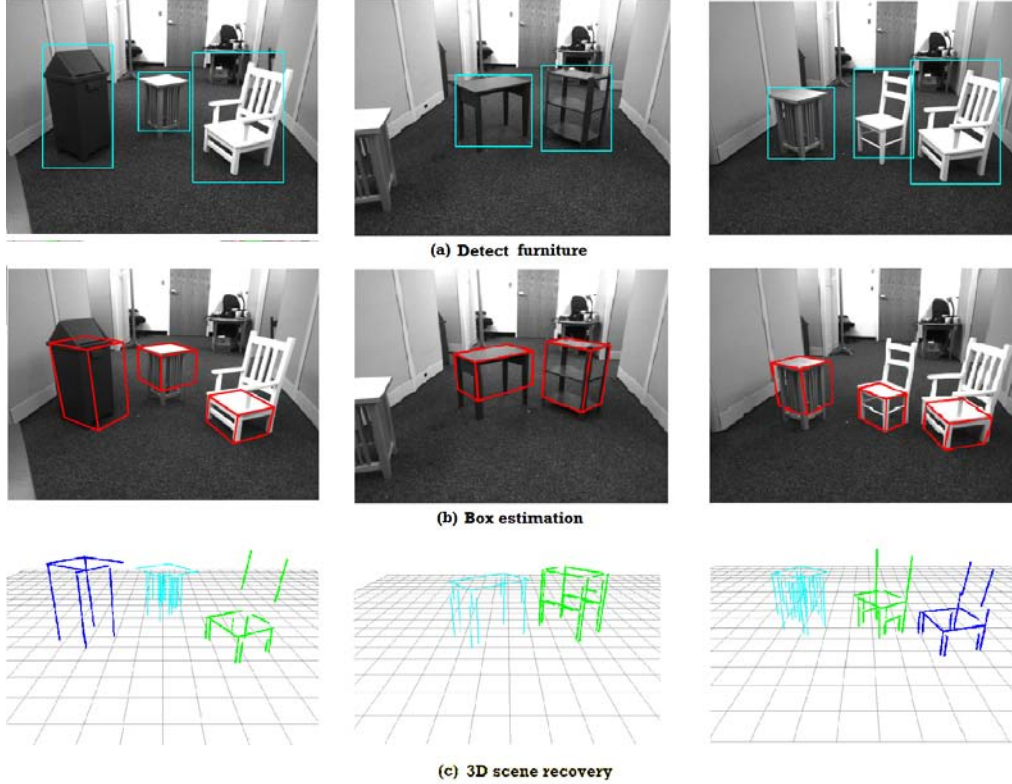


Fig. 9. (a) Detected objects. (b) Their 3D bounding boxes. (c) The recovered 3D shapes and locations.

Once the relevant 2D contours have been extracted for each of the 3D objects, two types of 3D representations can be produced, namely, a coarse representation of the 3D shape in the form of a rectangular bounding box (Figure 9b), and a more precise (finer) representation in the form of the 3D contours that represent each 3D shape (Figure 9c). How are the two representations computed? Consider the bounding box first. It can be computed by using three vanishing points (see Figure 10). One vanishing point is the intersection of symmetry lines (see Figure 5). The second vanishing point is the intersection of the lines in the 2D image that are projections of the vertical lines in the 3D scene. Note that in the presence of gravity, very many natural objects, such as cats, dogs, birds, and human beings, as well as furniture have appendages with multiple vertical edges we call their “legs”. Adjusting the orientation of these appendages permits them to maintain their balance when they stand or walk on tilted surfaces. This second vanishing point (which will be called here the “vertical vanishing point”) can be determined solely on the basis of information about the direction of gravity, information that is readily available to living creatures (see Figure 4). The vertical vanishing point is calculated as follows: Assume that the direction of gravity is N_g , then in the image the vanishing point for those 3D vertical lines can be expressed as:

$$v_g^* = MN_g \quad (9)$$

Equation (9) suggests that the vanishing point, like a horizon is determined by the camera's intrinsic properties and the camera's orientation. Finally, note that for many objects, such as furniture, there is a third vanishing point that represents the edges orthogonal to the other two types of edges in 3D (Figure 10). All three of these vanishing points form right angles with the vertex at the center of the perspective projection of the camera. This fact is equivalent to the following equation characterizing image properties (eq. 8.7 in Hartley & Zisserman, 2003):

$$v_i^{*T} K^{-T} K^{-1} v_j^* = 0 \quad i \neq j \quad (10)$$

The equation (just above) implies that if we know any two vanishing points, we can compute the third. In the case of animal bodies, which are not rectangular like chairs, the third vanishing point is also meaningful: it represents the direction in which the animal is facing. This means that a 3D rectangular bounding box computed on the basis of these 3 vanishing points is at least an adequate, albeit coarse representation for most objects, animate and inanimate.

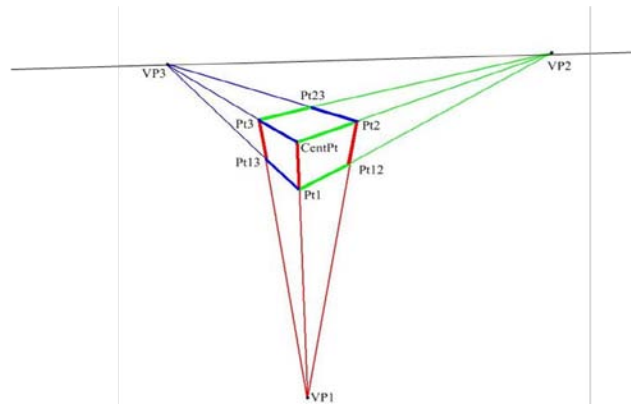


Figure 10. A perspective projection of a box. VP_1 , VP_2 and VP_3 represent the vanishing points for the three groups of mutually orthogonal line segments of the box.

Note that these 3D bounding boxes provide a type of information that is analogous to the way the boxes were estimated when we solved binocular FGO problem (see Figure 7b). The difference is that the boxes in Figure 7b were estimated on the basis of texture information, whereas the boxes in Figure 9b were estimated on the basis of contour information. One might consider the fact that these two different analyses led to the same result an instantiation of the action of Grossberg's feature and boundary contour systems (Grossberg & Mingolla, 1985). There is an important difference, namely, our analyses are taking place at the stage of the 3D representation, the stage at which the 3D objects actually reside.

A precise (fine) representation of the 3D shape can be produced by performing the 3D shape recovery on the basis of the object's symmetry (see Figure 9c). This recovery is done by using the algorithm described in Section 2. The only operation that remains to be

done is the detection of the 3D mirror symmetry in the 2D asymmetrical image. This operation is explained in Section 5.

5. Establishing the 3D symmetry correspondence of contours

A 2D image of a 3D mirror-symmetrical object is itself symmetrical but only for a narrow range of 3D viewing directions, so the question arises as to how a 3D symmetry can be detected in a 2D asymmetrical image. This problem is not trivial because pairs of unrelated 2D curves always have a 3D symmetrical interpretation (Sawada et al., 2011). In other words, without additional constraints, 3D symmetry is accidental. This fact is illustrated in <http://www1.psych.purdue.edu/~zpizlo/sym2011/DemoFiles/Demo8.html> where two different symmetrical interpretations of a 2D curve are given. One of these interpretations is natural in the sense that it agrees with the percept of an observer produced by a stationary 2D curve. The other interpretation is surprising. The difference between these two interpretations is that the natural interpretation consists of two planar curves. The fact that the human visual system uses a planarity constraint has been known at least since Leclerc & Fischler (1992) and Sinha & Adelson (1992) published their models, but it was less clear why a planarity constraint is actually used. Planar contours are quite common in man-made objects, but they are much less common in biological organisms. We believe that the human visual system uses the planarity of contours constraint because this constraint eliminates spurious symmetrical 3D interpretations rather than because planar contours are common. It is important to point out that the use of the planarity constraint does not imply that the 3D interpretations have planar contours; it only implies that the interpretations have contours that are biased towards planarity. This means that the torsion of 3D curves is kept to a minimum. It turns out that minimizing torsion eliminates 3D interpretations that correspond to degenerate views, views that preclude the veridical perception of 3D objects (Sawada et al., 2011).

If two 3D curves are planar and mirror symmetrical, their 2D images are related by a 2D affine transformation in the case of an orthographic image and by a 2D projective transformation in the case of a perspective image. The fact that a 3D symmetry can be detected in a 2D asymmetrical image through an application of a 2D transformation and its invariants simplifies the problem substantially. Under such conditions, 3D symmetry becomes non-accidental in the sense that a 2D image of a 3D asymmetrical shape is unlikely to have 3D symmetrical interpretations.

The task of detecting 3D symmetry in a 2D image is always simplified if higher order features, such as corners, intersections, complex curves and closed contours are detected first. Two pairs of feature points in a 2D image correspond to two pairs of mirror symmetrical points in a 3D interpretation only if the line segments connecting the 2D corresponding points are parallel in an orthographic image and if they intersect at a vanishing point in a perspective image. Recall from the section on 3D scene recovery that vanishing points and lines can be estimated directly from vestibular cues provided by gravity. The pictures at <http://web.ics.purdue.edu/~li135/SymDetect.html> show the result of establishing 3D symmetry correspondence for a few objects shown in 2D perspective images. In this example, our model checked whether any two junctions in the 2D images

satisfy the following two constraints: (1) the line connecting the junctions passes through one vanishing point and (2) the difference between two junction angles is equal to the sum of the angles formed by the two junctions with the other two vanishing points (see Figure 11b). These are the necessary conditions for a 3D symmetric interpretation in the case where the pair of symmetric curves are on parallel planes (like in the case of two sides of a chair shown in Figure 11a). The symmetrical pairs of curves are drawn in the same color. Once the contours have been organized, it is relatively easy to recover the 3D scene including the 3D shapes contained within it.

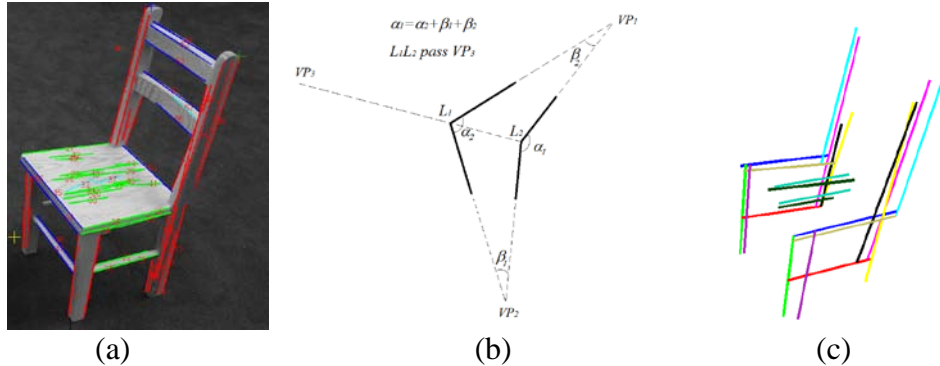


Figure 11. (a) Extracted curves for the image of a chair. Curves corresponding to the same vanishing points are drawn in the same color. (b) Two necessary conditions that are used to check whether the two edges of a junction are the potential symmetrical edges of another junction. (c) Detected symmetrical curves for the image in (a). Symmetrical curves are drawn in the same color.

6. Recovery of the top view of a 3D scene by human subjects.

The model results described in Section 3 imply that our model recovers a 3D scene very well. There is no sign of systematic errors and the random errors were not large. Is subjects' performance similar? We asked three subjects to draw the top views of 3D scenes and we compared the drawings to the ground truth provided by the PhaseSpace camera system (Appendix C). Below, we present the main aspects of the experimental method and of the results.

Methods

Subjects

Three subjects (TK, YS, and XZ) participated in the experiment. All observers had corrected-to-normal vision. TK was the author and XZ was a naïve subject.

Stimuli

The experiment was performed in a room (7.92 m × 8.53 m) illuminated by fluorescent lights on its ceiling. The walls were white with doors on two opposite sides. The floor was covered with blue, textureless carpet. An experimenter placed four or five pieces of children's furniture such as chairs, tables, bookshelves and garbage bins. They were

placed before each trial to form a scene without any occlusion from the point of view of the subject. An example of a typical scene used is shown in Figure 12.



Figure 11. A typical scene used in Experiment 1

The positions of objects were measured by PhaseSpace motion capture system (see Figure 13). The system is equipped with 16 pairs of cameras, each pair having two orthogonally oriented one-dimensional cameras. This system computes the 3D positions of multiple unique LEDs in a scene. The accuracy is better than 2 cm (see Appendix C for calibration details). In this experiment, one LED was put in the center of each object.

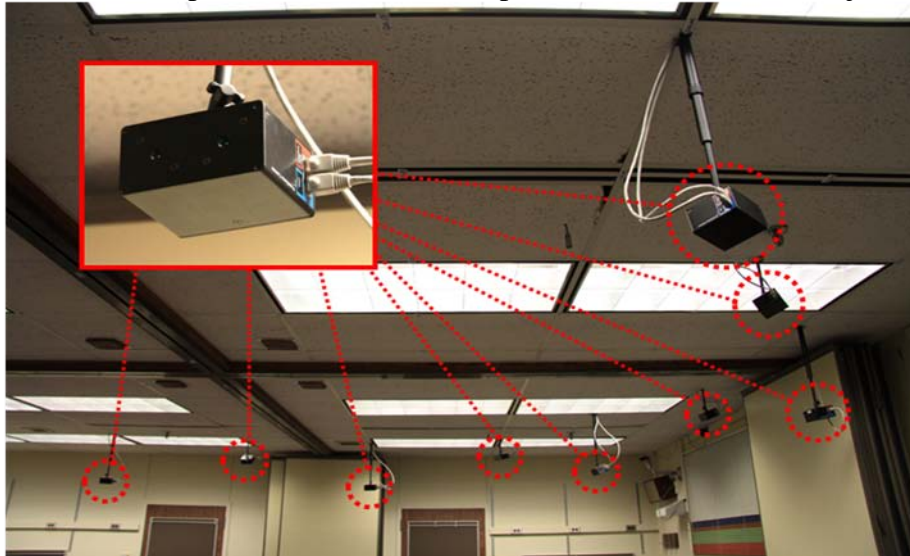


Figure 12. PhaseSpace motion capture system

Procedure

Each subject was tested in 40 trials (20 trials with binocular viewing and 20 trials with monocular viewing). The subject stood in a designated position viewing the scene. The subject reconstructed the scene on the tablet computer by dragging and dropping the ready-made icons (Figure 14). On the computer screen, there were icons which represented the shape and the relative size of each piece of furniture. The name tag was

placed on the bottom right corner of the icon. The subject was asked to drag and drop the icons with a pen to reconstruct the layout of the scene from a top view. The subject was instructed to use the sizes of the icons when deciding about the inter-object distances on the computer screen. The subject could rotate the icons to represent the orientation of objects.

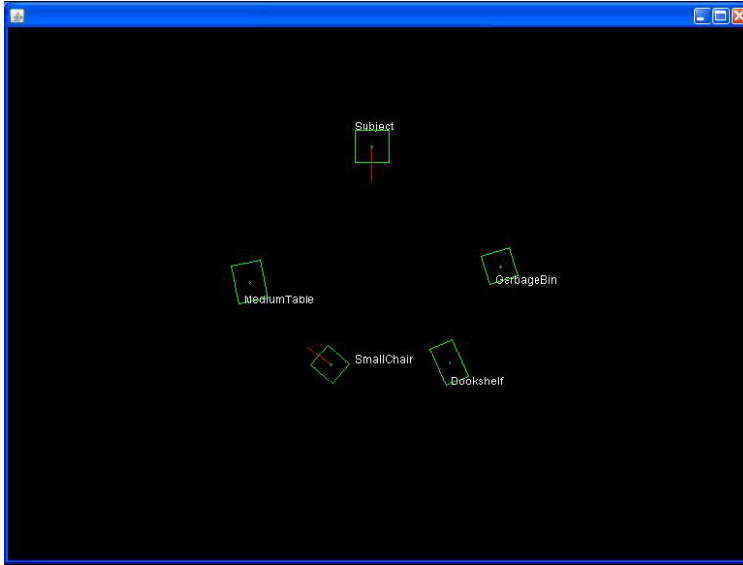


Figure 13. Interface on the tablet computer screen

Exposure duration was unlimited; the subject could look at the scene until he or she finished drawing the top view on the computer. After each trial, the experimenter put an LED on each object and recorded the LED positions by the PhaseSpace system. It took about 12 to 15 minutes to complete one trial. In half of the trials to the subject viewed the scene with two eyes. In the remaining half, the viewing was monocular (the left eye of the subject was occluded).

Results and Discussion

To evaluate how well the subject reconstructed the scene, the pairwise distances among all objects and the subject were computed. If there were n objects, $(n+1)*n/2$ pairwise distances were computed. The actual Euclidean distances among the centers of the objects were obtained by the PhaseSpace system which detects the positions of LEDs attached to the centers of the objects. The subject's reconstructed distances were obtained from the drawing on the tablet computer. The subject was instructed to scale the distances on the monitor by referring to the sizes of icons which represent the sizes of the physical objects. The mean squared error (MSE) for pairwise distances was estimated to evaluate the accuracy. The mean squared error is defined as follows:

$$MSE = E \left[\left(\frac{d' - d}{d} \right)^2 \right] \quad (11)$$

where d' is a reconstructed distance and d is an actual distance. The MSE is equal to the sum of the variance of normalized distances (d'/d) and the squared Bias:

$$\text{MSE} = \text{VAR}(d'/d) + \text{Bias}^2 \quad (12)$$

where $\text{Bias} = \mathbf{E} \left[\frac{d' - d}{d} \right]$. Taking the square root of MSE and VAR yields the root-mean-square (RMS) error and standard deviation (STD) which have the unit of % of actual distance:

$$\text{RMS} = \sqrt{\text{MSE}} \quad (13)$$

$$\text{STD} = \sqrt{\text{VAR}} \quad (14)$$

Table 1 shows these errors calculated for each subject.

Table 1. Monocular and binocular errors of Subject's Reconstruction in Experiment 1

Subject	Viewing condition	RMS(%)	STD(d/d) (%)	Bias(%)
TK	Monocular	20.20	19.70	4.64
TK	Binocular	13.79	12.65	-5.56
YS	Monocular	21.99	15.96	15.17
YS	Binocular	20.71	15.27	14.03
XZ	Monocular	27.16	21.80	16.26
XZ	Binocular	24.72	21.13	12.88

The RMSs of these pairwise distances ranged from 13% to 27%. It can be seen that the Bias was quite large in the case of YS and XZ. They systematically overestimated distances. The TK's Bias, computed from all 20 monocular and all 20 binocular trials was close to zero. But this does not necessarily mean that his Bias was close to zero in individual trials. The analysis of the nature of Bias is important because it may shed light on the question as to whether the source of Bias is related to perception or response bias. The subjects were asked to scale the distances on the monitor by using the sizes of icons representing the objects as reference. Note, however, that the inter-object distances were an order of magnitude larger than the objects themselves. This is very similar to the conventional size constancy task, which is known to lead to large variability (Brunswik, 1944). It is possible that after the subject set the first distance, he used this distance as a reference to decide about the remaining distances. This way the subject would avoid comparing distances and sizes of very different magnitudes. If subject used this approach in reconstructing the scene, then all distances within a given trial would share the same systematic error. This, in turn, implies large random fluctuation of Bias across trials. Figure 15 shows histograms of the intra-trial Bias for monocular and binocular viewing.

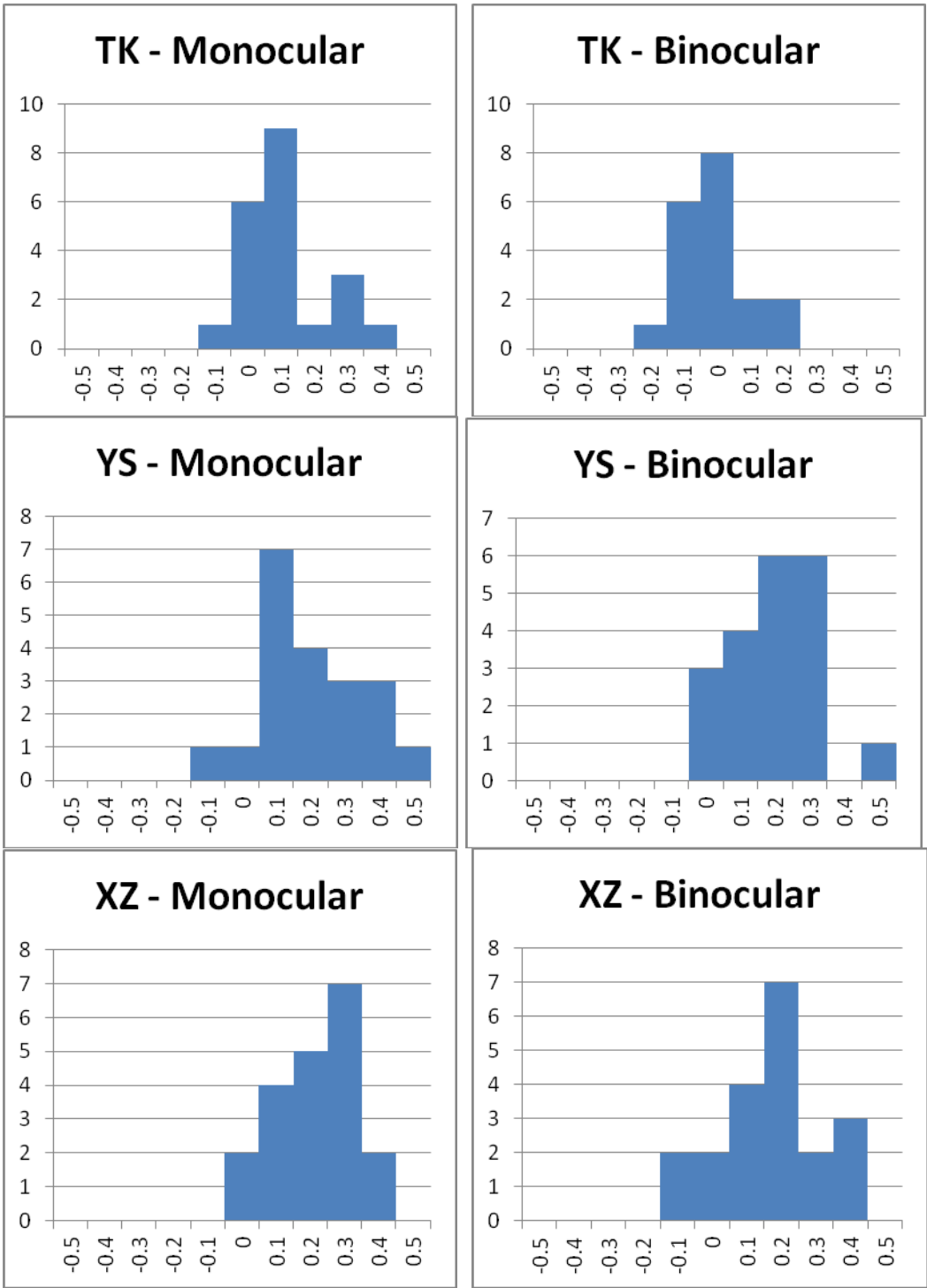
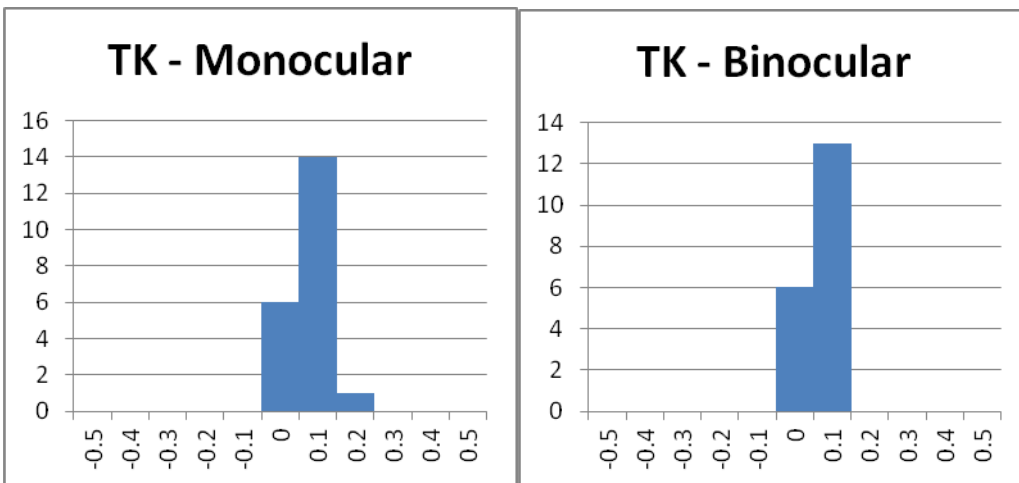


Figure 14. Histogram of the intra-trial Bias of three subjects (TK, YS and XZ) in monocular and binocular viewing

The intra-trial Bias varied from -0.1 to 0.5. This variability of Bias contributed to large values of MSE and VAR. Note that the fact that the Bias is similar in monocular and binocular viewing suggests that it is caused by response bias, rather than by perceptual distortions.

Next, we evaluated the source of Bias. If Bias is caused by the difficulty in scaling the distances in each trial (as suggested above), then Bias would go away after the reconstructed space is scaled in each trial. But it is also possible that Bias is caused by distortions of the visual space, such as affine or projective. The presence of such distortions will be verified by applying transformations to the reconstructed top views and verifying whether the distances among transformed positions of objects are closer to the true distances. We begin with size scaling and rotation of the reconstructed map. Specifically, the best rotation and size scaling in the least squares sense was applied independently to individual trials. Rotation is needed because there is no reason to assume that the orientation on the computer screen was identical to the orientation in the room. In other words, the subject did not try to match directions of the walls in the room with directions of the frame of the computer monitor. The center of the scaling and rotation was placed at the subject's position. Size scaling removed the intra-trial Bias discussed in the previous paragraph. This is illustrated in Figure 16, which shows histogram of intra-trial Bias after size scaling. Specifically, the variance of the intra-trial Bias decreased by a factor of X , Y and Z for TK, YS and XZ, respectively.



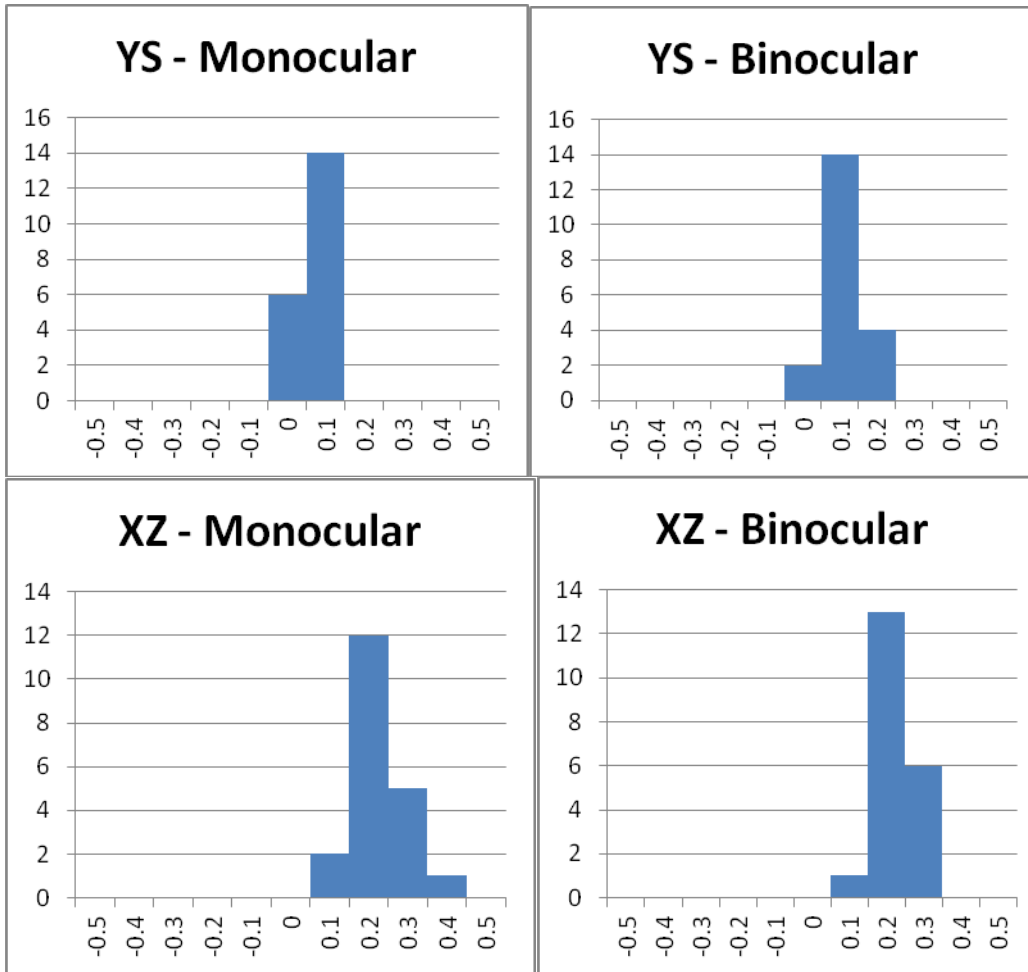


Figure 15. Histogram of the intra-trial Bias of three subjects (TK, YS and XZ) in monocular and binocular viewing after size scaling

In addition to this Euclidean transformation, the affine and projective transformations were also applied to the reconstructed positions to all trials. If the affine or projective mapping represents perceptual bias, then affine or projective transformation will reduce the errors substantially. All transformations were optimal in the least square sense. Table 2 shows all the transformations that were used. Note that the translation is not explicitly shown in Table 2. Translation was performed as the first step, by assuming that the physical position of the subject coincided with the position of the icon representing the subject on the computer screen.

Table 2. Transformations applied to the reconstructed positions

Transformation	Equation
Euclidean transformation	$x' = a\{x \cos \theta - y \sin \theta\}$ $y' = a\{x \sin \theta + y \cos \theta\}$
Affine transformation (with two parameters)	$x' = bx$ $y' = cy$

Affine transformation
(with four parameters)

$$\begin{aligned}x' &= dx + ey \\y' &= fx + gy\end{aligned}$$

Projective transformation
(with two parameters)

$$\begin{aligned}x'' &= \frac{x'}{hx' + iy' + 1} \\y'' &= \frac{y'}{hx' + iy' + 1}\end{aligned}$$

Projective transformation with 2 parameters was applied to the data after the affine transformation with 2 parameters to simplify the analysis. Projective transformation after affine transformation with 4 parameters was also applied and showed similar results. The effect of the individual transformations was evaluated by computing standard deviation of the normalized distance across 20 trials. The random errors, as measured by standard deviation of the normalized distance, show no systematic difference between monocular and binocular viewing. In particular, for TK and XZ, binocular viewing led to better performance, while the opposite was true for YS. As we can see, errors decreased substantially when rotation and scaling were applied. In fact, scaling was the main source of error because rotation does not affect the pairwise distances. Further transformations such as affine and projective did not affect errors much. This implies that the human visual space is likely to be Euclidean, rather than affine or projective, as prior research suggested. This way, we confirmed that the 3D vision of our machine is similar to the 3D vision of our subjects.

So, how do we explain the fact that human subjects perceive the layout on the floor so well? There is no systematic error, and the random variability is quite small. The explanation turns out quite simple, computationally, once we recognize the operation of several effective a priori constraints: (i) gravity, (ii) horizontal floor on which all objects reside, and (iii) known height of subject.

(i) It is known that humans are able to judge the direction of gravity with threshold less than 1 deg (Garten ,1920, Neal, 1926, Skavenski, et. al. 1979).

(ii) The fact that all objects reside on the common horizontal floor allows one to reconstruct the positions of all objects even using information provided by one eye, only.

(iii) In order to solve the triangle (Figure 17), the subject has to know his own height. This will allow the subject to reconstruct the layout of the scene, *depths* of all objects, and all pairwise distances without using any *depth cues*. Recall that using depth cues leads to large distortions of the visual space. When effective *a priori constraints* are substituted for depth cues, the visual space becomes Euclidean.

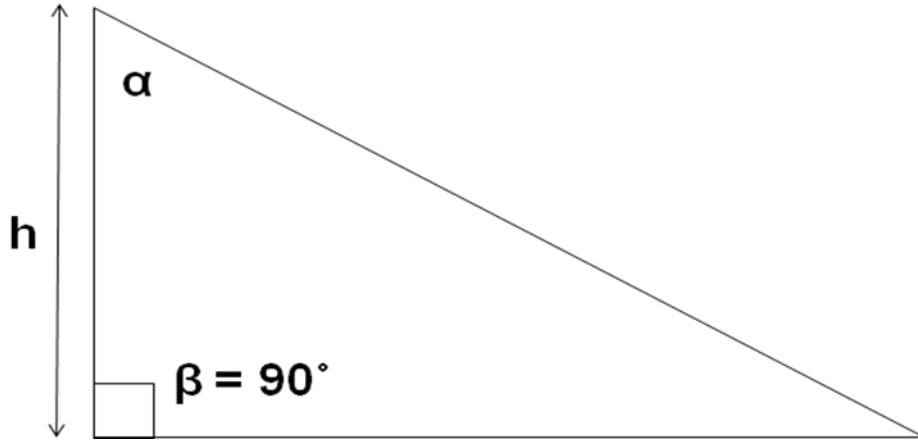


Figure 17. Assume that the standard deviation of judging the angles α and β relative to gravity is 1 deg. α represents the angle between the eye and the direction of gravity, and β represents the angle between the subject's vertical body and the horizontal floor. Assume that these two judgments are independent. For the viewing distance of 2m (like in the Experiment), the predicted standard deviation of distance judgment is 5%, which is close to what we measured.

Summary and Conclusion

We developed a set of computational tools (models) that allow a robot to “see” a natural 3D scene and to “understand” it in the sense that it can recover the 3D shapes, sizes and locations of the objects in the scene as well as the free spaces among them. The Figure-Ground Organization and 3D shape recovery tools built into our robot permits it to perform both of these complicated tasks on its own. Despite considerable progress, there is still a lot of work to be done. By far, the most important unfinished business is to implement the algorithms in such a way that the model does its visual processing in “real time” as defined by the temporal processing characteristics of the human and other biological systems. Once these computations are performed in real time, the next step will be to implement computational models of motion perception. This will allow the robot to deal with dynamic environments as well as we do. Last, but by no means the least task facing us, the models currently used for extracting all relevant contours of 3D shapes should be elaborated so that the robot can extract 3D shapes and scenes with the high degree of precision characteristic of the human visual system. Note that all of these unfinished projects are actually elaborations of the 3D shape and scene recovery models that we have in hand now. In other words, all of the major steps required for 3D shape and scene recovery have been accomplished and they can be performed autonomously by a robot at this time. The remaining steps (described just above) are designed to enhance its performance, bringing it in line with the performance of human beings. Once they are accomplished, our robot will not only be able to act autonomously; it will also be able to navigate within natural scenes as well as a human being can navigate under similar conditions. There is even good reason to believe that the FGO and 3D shape-recovery tools that we have seen work so well for our robot are actually rather similar to those used by human beings performing similar tasks. We feel entitled to make this claim because

when we tested these tools in human psychophysical experiments, the human and the model's performances were very similar (Kwon et al., 2011; Li et al., 2011). Even if we ignore this psychophysical support, the mere fact that the robot can actually "see" a 3D scene veridically and plan its actions effectively within it, provides evidence for our belief that the robot's tools are at least biologically-plausible even if they ultimately prove to be different from those actually used in the human visual system. It is important in evaluating these provocative claims to keep in mind that no other existing machine vision system has even come close to approximating the performance of the human being in even very simple visual environments. Our machine vision system approximates human performance very well in relatively complex, naturalistic environments. Discovering that a system like ours can do this provided us with some new insights into how a visual system like ours accomplishes what it does so well. Finally, explaining how the human visual system works has been only one of the goals of our work.

It has not gone unnoticed that robots, equipped with the novel kind of computational visual system described in this report, will be able to deliver food and supplies in hospitals and trim grass on lawns at least as well as conventional contemporary robots can perform such tasks, but conventional robots, unlike ours, accomplish these tasks by using tools that do not resemble those used by human beings. Our robot's tools do and this fundamental difference opens up the possibility of having a machine emulate a wide range of human activities within quite complex natural environments. This becomes possible because our machine and human beings perform effective navigations without measuring absolute distances. Both navigate by constructing a limited number of accurate representations of 3D shapes. All other contemporary robots base their navigations on making many iterative measurements of absolute distances. The simple visual/gravitational method used by our machine for FGO, 3D shape and 3D scene recovery probably works so well because it emulates the method that human beings, and many other successful animals, honed during the millennia required for their evolution.

Appendix A: The recovery of a pair of symmetrical points

Suppose x is a point in a 2D image and it is expressed by Euclidean coordinates. Its corresponding homogenous coordinates can be written as

$$x^* = \begin{pmatrix} x^T & 1 \end{pmatrix}^T \quad (\text{A1})$$

Suppose M is a 3x3 matrix that consists of the first three column vectors of a camera matrix and p_4 is the fourth column vector of the camera matrix. Then all 3D points whose image is x is expressed as follows (Hartley & Zisserman, 2003)

$$X = M^{-1}(kx^* - p_4) \quad (\text{A2})$$

in which k is a free parameter. Note that X is a vector with the Euclidean coordinates of a 3D point. Suppose X_1 and X_2 are a pair of symmetric 3D points, their images are x_1 and x_2 . Then from Equation A2, we obtain

$$X_i = M^{-1}(k_i x_i^* - p_4) \quad i = 1, 2 \quad (\text{A3})$$

Therefore, to recover the 3D point X_1 and X_2 from their images x_1 and x_2 , we need to compute k_1 and k_2 in Equation A3. Suppose the direction of the line X_1X_2 is V , then V and v^* must satisfy the following equation

$$V = M^{-1}v^* \quad (\text{A4})$$

Note that V represents not only the direction of X_1X_2 , but also the normal of symmetry plane. Therefore the symmetry plane for X_1 and X_2 can be expressed as

$$\pi = \begin{pmatrix} V^T & d \end{pmatrix}^T \quad (\text{A5})$$

where d indicates the position of the symmetry plane.

X_1 and X_2 are symmetric with respect to the symmetry plane π if and only if the following two conditions are satisfied

- (1) the line X_1X_2 is perpendicular to the symmetry plane π ;
- (2) the midpoint of X_1 and X_2 is on the symmetry plane π .

From condition (1), we can derive

$$X_1 - X_2 = k_v V \quad (\text{A6})$$

Combining equation A6 with equations A3 and A4, we obtain

$$M^{-1}(k_1 x_1^* - p_4) - M^{-1}(k_2 x_2^* - p_4) = k_v M^{-1}v^* \quad (\text{A7})$$

Left multiplying by M both sides of the equation A7, we obtain

$$k_1 x_1^* - k_2 x_2^* = k_v v^* \quad (\text{A8})$$

Replacing the homogenous coordinates for x_1 , x_2 and v in equation A8 with their Euclidean coordinates, we obtain

$$k_1 \begin{pmatrix} x_1 \\ 1 \end{pmatrix} - k_2 \begin{pmatrix} x_2 \\ 1 \end{pmatrix} = k_v \begin{pmatrix} v \\ 1 \end{pmatrix} \quad (\text{A9})$$

It follows

$$k_v = k_1 - k_2 \quad (\text{A10})$$

Replacing k_v in equation A9 with the expression in equation A10, we obtain

$$k_1(x_1 - v) = k_2(x_2 - v) \quad (\text{A11})$$

Equation A11 implies two facts

- (a) x_1 , x_2 and v are collinear. Thus, equation A11 is redundant.
- (b) the ratio between k_1 and k_2 is proportional to the ratio of the vectors x_2v and x_1v .

Because x_1 and x_2 must be on the same side of v , equation A11 can be written as

$$k_1|x_1 - v| = k_2|x_2 - v| \quad (\text{A12})$$

where $|x_1 - v|$ and $|x_2 - v|$ represent the distance from x_1 and x_2 to v . Equation A12 suggests that the ratio of k_1 and k_2 is proportional to the ratio of distance from two symmetric points to the vanishing point.

From condition 2, we can derive

$$\frac{X_1 + X_2}{2}V + d = 0 \quad (\text{A13})$$

Combining equation A13 with equations A3 and A4, we obtain

$$\begin{pmatrix} v^{*T}M^{-T}M^{-1}x_1^* & v^{*T}M^{-T}M^{-1}x_2^* \end{pmatrix} \begin{pmatrix} k_1 \\ k_2 \end{pmatrix} = 2v^{*T}M^{-T}M^{-1}p_4 - 2d \quad (\text{A14})$$

Combining equations A12 and A14, we obtain

$$\begin{pmatrix} v^{*T}M^{-T}M^{-1}x_1^* & v^{*T}M^{-T}M^{-1}x_2^* \\ |x_1 - v| & -|x_2 - v| \end{pmatrix} \begin{pmatrix} k_1 \\ k_2 \end{pmatrix} = \begin{pmatrix} 2v^{*T}M^{-T}M^{-1}p_4 - 2d \\ \bar{0}_{2 \times 1} \end{pmatrix} \quad (\text{A15})$$

Appendix B: Estimating the vanishing point on a horizon from a set of symmetry lines

Let the horizon be expressed as

$$l^* = (l_x \quad l_y \quad l_w)^T \quad (\text{B1})$$

then $v_0^* = (-l_y \quad l_x \quad 0)^T$ and $v_1^* = (0 \quad -l_w \quad l_y)^T$ ⁶ are two points on the horizon because $l^{*T}v_0^* = 0$ and $l^{*T}v_1^* = 0$. Specifically v_0^* is a point at infinity on the horizon. Then all points on l^* can be expressed as

$$v^* = v_0^* + \lambda v_1^* \quad (\text{B2})$$

Let $l_1^*, l_2^*, \dots, l_k^*$ represents the k symmetric lines. Ideally, if all symmetric lines intersect with the horizon at point v^* , then the following equations will be satisfied

$$l_i^{*T}v^* = 0 \quad i=1,2,\dots,k \quad (\text{B3})$$

Let $B = (l_1^{*T} \quad l_2^{*T} \quad \dots \quad l_k^{*T})^T$, then equation B3 is expressed as

$$Bv^* = \vec{0}_{k \times 1} \quad (\text{B4})$$

Combining equations B2 and B4, we obtain

$$\lambda Bv_1^* = -Bv_0^* \quad (\text{B5})$$

Therefore, the problem of estimating the vanishing point on the horizon is changed to finding the optimum value of λ that satisfies equation B5 in the least square sense. It follows

$$\lambda = ((Bv_1^*)^T (Bv_1^*))^{-1} (Bv_1^*)^T (-Bv_0^*) \quad (\text{B6})$$

or

$$\lambda = -\frac{v_1^{*T} B^T B v_0^*}{v_1^{*T} B^T B v_1^*} \quad (\text{B7})$$

⁶ If l_y is 0, then v_0^* and v_1^* represent the same point. For this case, we can set $v_1^* = (-l_w \quad 0 \quad l_x)^T$. If both l_x and l_y are 0, then l^* represents the line at infinity and it is the vanishing lines for the planes that are parallel to the image plane. For this case, we can set $v_0^* = (1 \quad 0 \quad 0)^T$ and $v_1^* = (0 \quad 1 \quad 0)^T$.

Appendix C. Calibration of PhaseSpace System

The PhaseSpace motion and position capture system was calibrated with regard to the physical space. What is “calibration”? It is a process matching the coordinate of the system with that of the physical space. The coordinate in the physical space was defined by drawing a rectangular grid with 1m steps on the floor. Then, the positions of the vertices of the grid were measured by PhaseSpace system and the transformation between the two coordinate systems was derived.

The positions on the grid of 5 m by 5 m square on the floor were measured by PhaseSpace system and the accuracy of the measurements was evaluated in the following way.

Drawing the grid on the floor

The grid was drawn in the following steps: first, a 5 m by 5 m square was drawn on the floor and the square was divided with 1 m steps.

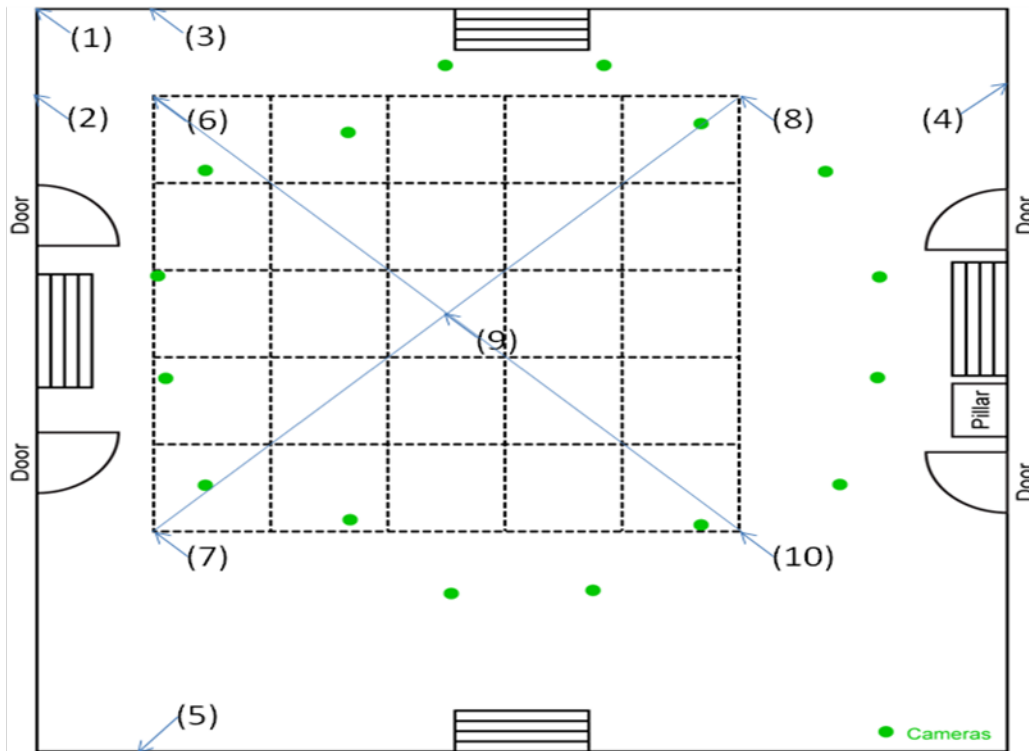


Figure C6. Map of the room to indicate the position of grids, cameras and surrounding objects. Some important points are labeled with numbers in parenthesis.

After that, the strings were placed on the floor to connect the four corners of the 5 m by 5 m square. Lasers were used to make sure that the strings are straight in the right direction. The strings were fixed by duck tapes next to the points. Then the 5 m lines were divided into 5 intervals of 1 meter steps by tape measure. Checking the accuracy of intersection, the strings were placed to make 25 of 1 m by 1 m squares. All intersection points were marked with triangular shape tape. The 5 m by 5 m square with 1 m step strings were placed on the floor of the room.

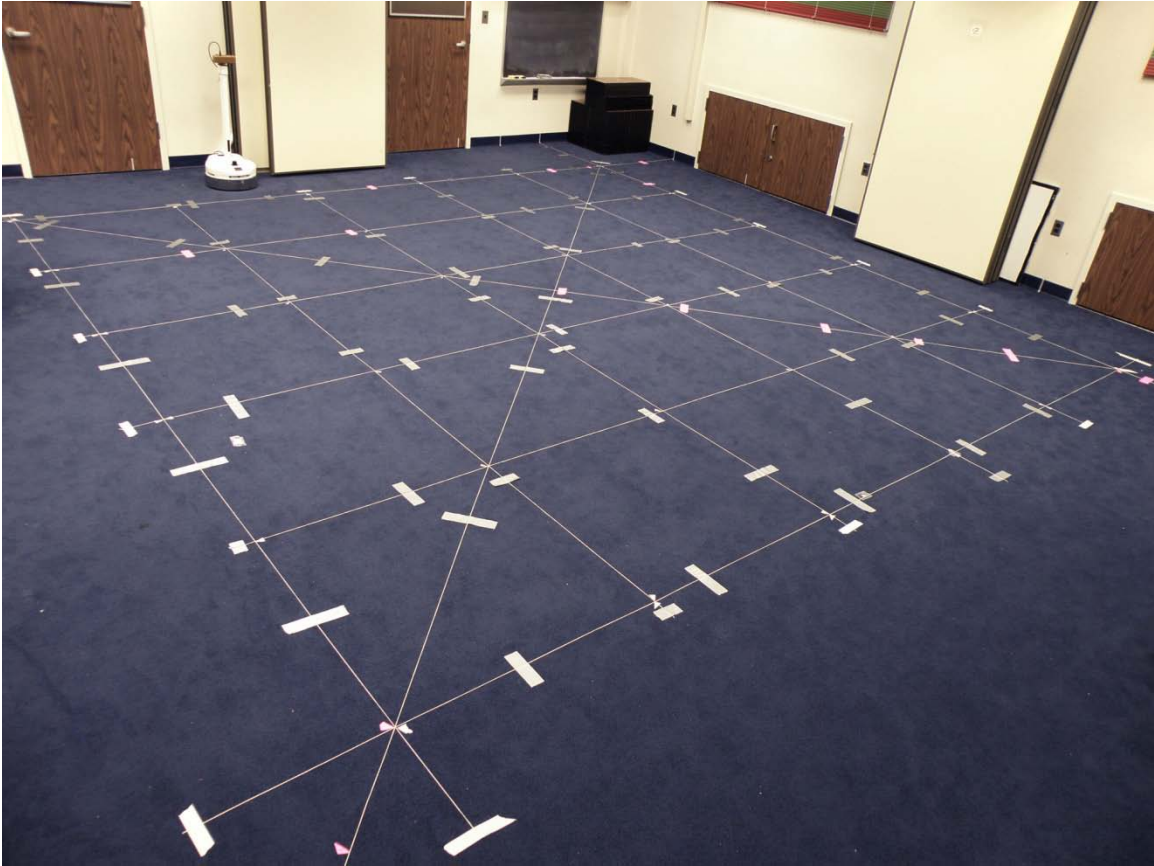


Figure C7. The grids of 1 m steps on the floor were drawn with strings. Two diagonals were also drawn to use it as a hypotenuse of two triangles.

Comparing the coordinate systems of the physical space and the PhaseSpace system

Recording the 3D positions of 1 m step grids

The positions of the points in the physical coordinate system were measured using the PhaseSpace system. The positions of the measured points were at the vertices of the grid on the floor and 60 cm above the vertices of the grid. The positions were recorded by the system 300 times for 10 seconds (30Hz). The positions of all vertices of the grid were measured with PhaseSpace system. At first, LEDs were placed on every point on the floor level and recorded for about 10 seconds. After that, an LED was attached to the 60 cm height bar. By putting the bar on each point on the floor, the positions of intersection points at 60 cm height level were measured for about 10 seconds, too. The system recorded the positions 30 times a second.

Finding stable and reliable points

Although most recorded data were stable across the recorded time, there was some fluctuation across the recorded time. The graphs in Figure 3 show that the ranges of measurement in one position for 10 seconds. The ranges were computed by subtracting the minimum measurement from the maximum measurement. As shown in the graphs in Figure 3, the measurements around the centers were stable. However, the measurements around the edges of the square were unstable showing bigger ranges up to 32 mm.

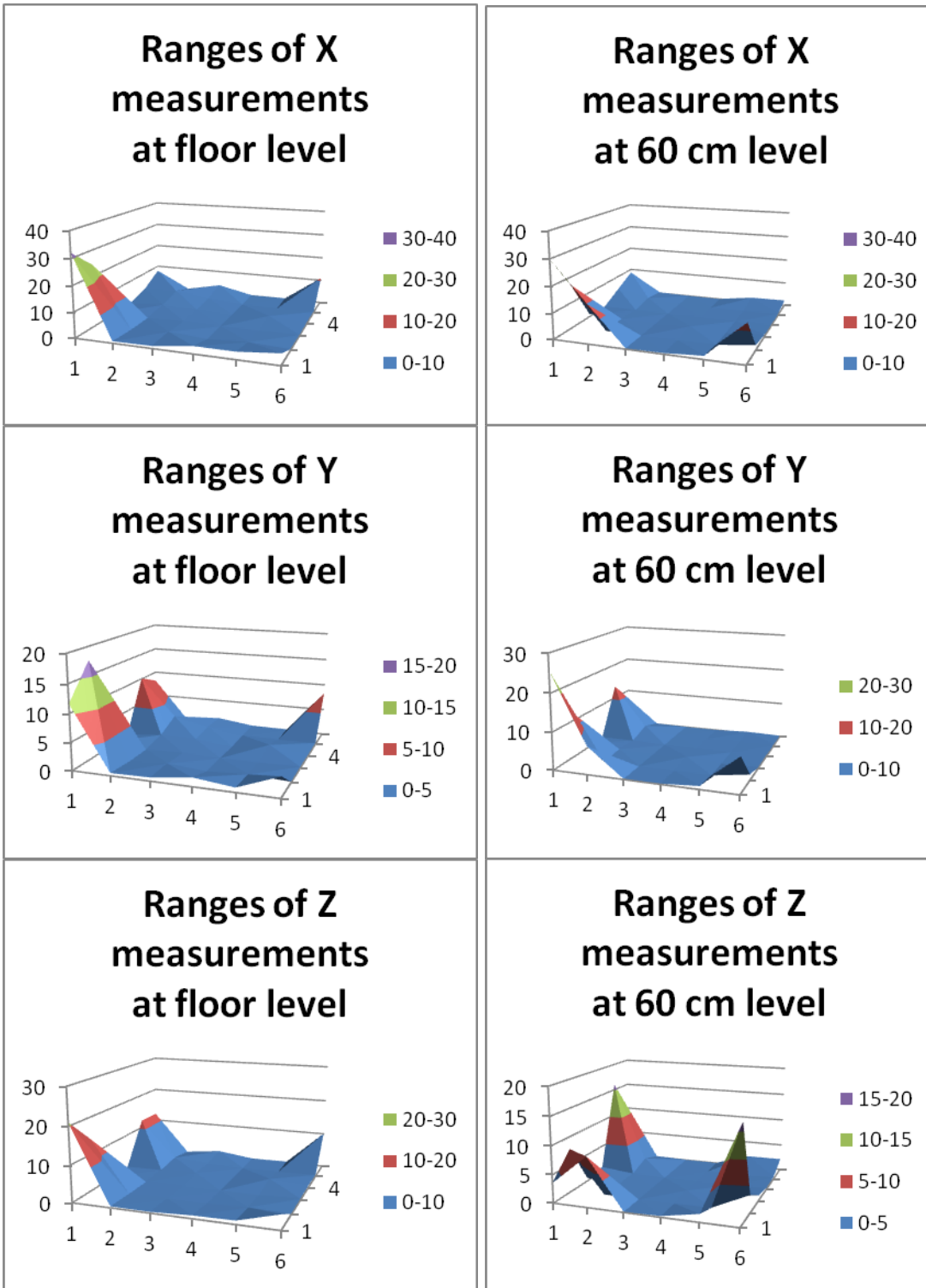


Figure C8. The ranges of measurements in one position across the 5 m by 5 m square for 10 seconds.

Most unstable points were located in row 1 or column 1 which were farthest from the center of a circle of cameras. Note that these points could be observed only by the cameras which are placed on the opposite side of the circle and are far from the points. The cameras above the points could not see the points because of the limited viewing angle of the cameras, which are oriented to the center of the circle. Hence, small sampling

error in the computation causes the bigger error. If those points were removed, the errors should have decreased close to zero. Actually, after excluding the data of row 1 and column 1, the maximum ranges were within 2.3 mm.

Finding the transformation between physical space and measured space

Now, the measurements on each point across time were averaged to represent a single 3D coordinate for each point. The best 3D transformation between the two coordinate systems of the physical space and the PhaseSpace system was derived by minimizing the Euclidean distance between the physical positions and the output of the PhaseSpace system. Here, the least square method was used. The 3D transformation includes translation in x, y and z axis direction, rotation around x, y, and z axis, and homogeneous size scaling. In total, there were 7 free parameters. The maximum error of the Euclidean distance between physical grid and transformed grid turned out to be 19.9 mm.

The errors of the x-, y- and z-coordinates were plotted in Figure 4. The errors were computed by subtracting the physical position from the measured position after the transformation. Below are the graphs of X, Y, and Z axis errors.

After these calibration procedures, the PhaseSpace system could detect the 3D position within the maximum error of 2 cm.

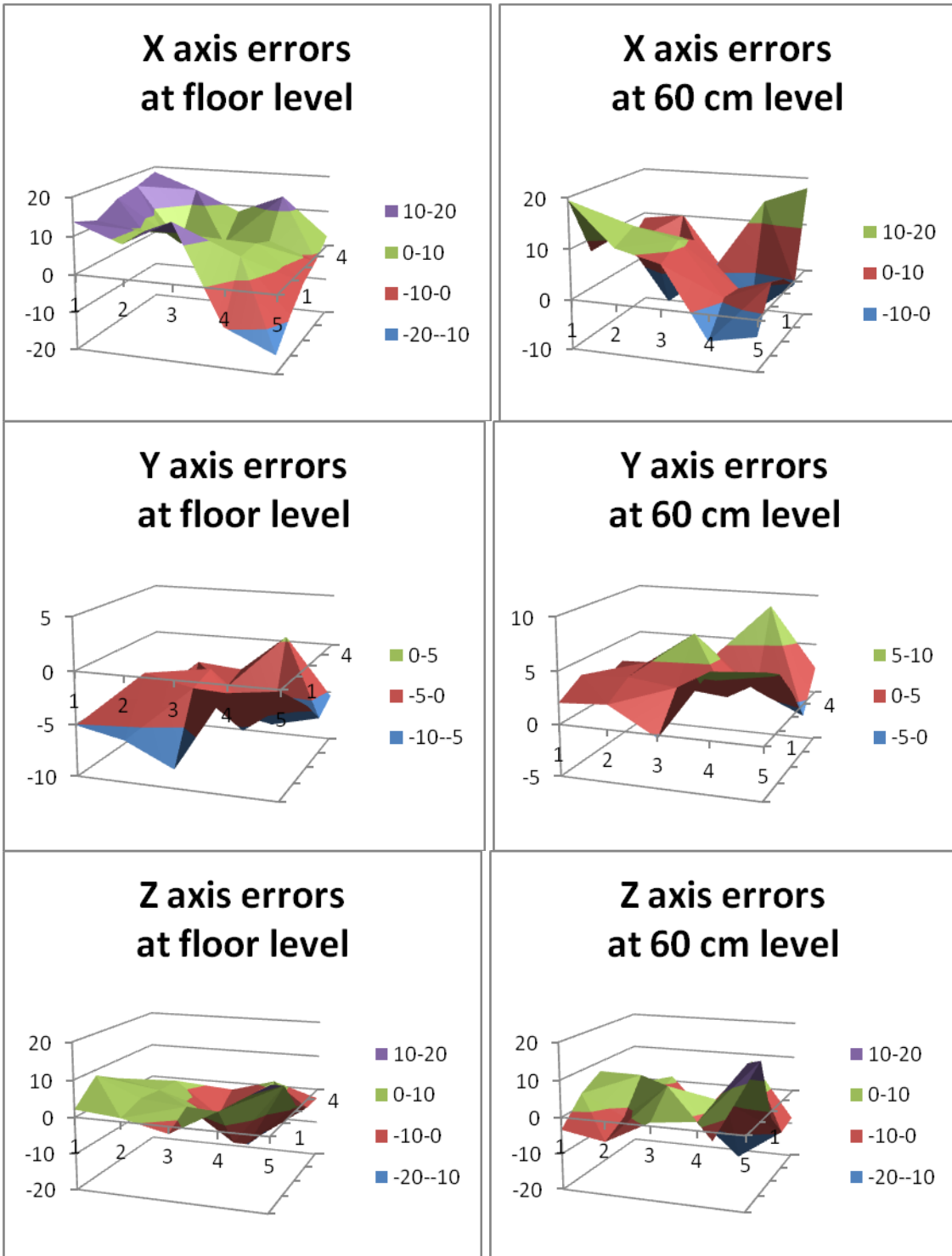


Figure C9. The errors of the x-, y- and z-coordinates at both floor level in the left column and 60 cm level after transformation

References

- Andriluka, M., Roth, S., and Schiele, B. (2008) People-tracking-by-detection and people-detection-by-tracking. CVPR 2008.
- Attneave, F. & Frost, R. (1969) The determination of perceived tridimensional orientation by minimum criteria. *Perception & Psychophysics*, 6, 391-396.
- Bartlett, F. (1932) Remembering. Cambridge: Cambridge University Press.
- Dewey, J. (1896) The reflex arc concept in psychology. *Psychological Review*, 3, 357-370.
- Faugeras, O. (2001) *Three-dimensional computer vision – a geometric viewpoint*. Cambridge, MA: MIT Press.
- Ferrari, V., Tuytelaars, T., and Gool, L. V. (2006) Object detection with contour segment networks. *ECCV*, 2006.
- Gibson, J. J. (1966) *The senses considered as perceptual systems*. Boston: Houghton Mifflin.
- Grossberg, S. & Mingolla, E. (1985). Neural dynamics of form perception: Boundary completion, illusory figures, and neon color spreading. *Psychological Review*, 92, 173-211.
- Hartley, R. & Zisserman, A. (2003) *Multiple view geometry in computer vision*. Cambridge: Cambridge.
- Hebb, D. O. (1949) *The organization of behavior*. New York: Wiley.
- Kubovy, M. (1986) *The Psychology of Perspective and Renaissance Art*. Cambridge: Cambridge University Press, 1986.
- James, W. (1890) *The principles of psychology*. New York: Dover.
- Julesz, B. (1971) *Foundations of cyclopean perception*. Chicago: University of Chicago Press.
- Kwon, T., Shi, Y., Li, Y., Sawada, T. & Pizlo, Z. (2011) Natural and virtual scenes: human recovery of the shape of a 3D scene. *Journal of Vision*, 11(11): 72 (VSS Abstract).
- Latecki, L.J., Lu, C., Sobel, M. & Bai, X. (2008) Multiscale Random Fields with Application to Contour Grouping. *Neural Information Processing Systems Conf. (NIPS)*, 2008.
- Leclerc, Y. G. & Fischler, M. A. (1992) An optimization-based approach to the interpretation of single line drawings as 3D wire frames. *International Journal of Computer vision*, 9, 113-136.
- Li, Y. (2009). Perception of Parallelepipeds: Perkins' Law. *Perception*, 38, 1767-1781.
- Li, Y. & Pizlo, Z. (2011) Depth cues vs. simplicity principle in 3D shape perception. *Topics in Cognitive Science* 3, 667-685.
- Li, Y., Pizlo, Z., & Steinman, M. R. (2009). A computational model that recovers the 3D shape of an object from a single 2D retinal representation. *Vision Research*, 49, 979-991.
- Li, Y., Sawada, T., Shi, Y., Kwon, T. & Pizlo, Z. (2011) A Bayesian model of binocular perception of 3D mirror symmetrical polyhedral. *Journal of Vision*, 11(4):11 1-20.
- Lin, Z., Hua, G., and Davis, L. S. (2009) Multiple instance feature for robust part-based object detection. *CVPR* 2009.

- Ma, T. & Latecki, L.J. (2011) From Partial Shape Matching through Local Deformation to Robust Global Shape Similarity for Object Detection. *IEEE Conf. on Computer Vision and Pattern Recognition (CVPR)*, June 2011.
- Marr, D. (1982) *Vision*. San Francisco: W.H. Freeman.
- Miller, G. A., Galanter, E. & Pribram, K. H. (1960) *Plans and the structure of behavior*. New York: Holt.
- Pirenne, M. H. (1970) *Optics painting & photography*. London: Cambridge.
- Pizlo, Z. (2001) Perception viewed as an inverse problem. *Vision Research*, 41, 3145-3161.
- Pizlo, Z. (2008). *3D shape: Its unique place in visual perception*. Cambridge, MA: MIT Press.
- Pizlo, Z., Sawada, T., Li, Y., Kropatsch, G. W & Steinman, M. R. (2010). New approach to the perception of 3D shape based on veridicality, complexity, symmetry and volume. *Vision Research*, 50, 1-11.
- Poggio, T., Torre, V. & Koch, C. (1985) Computational vision and regularization theory. *Nature*, 317, 314-319.
- Sawada, T. (2010) Visual detection of symmetry in 3D shapes. *Journal of Vision*, 10(6):4, 1-22
- Sawada, T. & Pizlo, Z. (2008) Detection of skewed symmetry. *Journal of Vision*, 8(5):14, 1-18.
- Sawada, T., Li, Y. & Pizlo, Z. (2011) Any pair of 2D curves is consistent with a 3D symmetric interpretation. *Symmetry* 3, 365-388.
- Sawada T., Li Y. & Pizlo Z. (2011) Symmetry, shape, surfaces, and objects. In C. W. Tyler (Ed.), *Computer Vision: From Surfaces to 3D Objects* (pp. 113-124). Boca Raton, FL: Chapman Hall/CRC.
- Sinha, P. & Adelson, E. H. (1992) Recovery of 3-D shape from 2-D wireframe drawings. *Investigative Ophthalmology & Visual Sciences*, 33 (Suppl.), 825.
- Srinivasan, P., Zhu, Q. & Shi, J. (2010) Many-to-one contour matching for describing and discriminating object shape. *CVPR*, 2010.
- Steinman, R. M. (1965) Effect of target size, luminance and color on monocular fixation. *Journal of the Optical Society of America*, 55, 1158-1165.
- Toshev, A., Taskar, B. & Daniilidis, K. (2010) Object detection via boundary structure segmentation. In *IEEE Comp. Vision Pattern Recognition (CVPR)*.
- Troscianko, T., Benton, C.P., Lovell, P.G., Tolhurst, D.J. & Pizlo, Z. (2009) Camouflage and visual perception. *Philosophical Transactions of the Royal Society B* **364**, 449-461.
- Troscianko, T., Benton, C.P., Lovell P.G., Tolhurst, D.J. & Pizlo, Z. (2011) Camouflage and visual perception. In: M. Stevens & S. Merilaita (Eds.), *Animal Camouflage: Mechanisms and Function*, Cambridge University Press (pp. 118-144).
- Wong, S., Vassiliadis, S., & Cotofana, S. D.. (2002) A sum of absolute differences implementation in hardware. *Proceeding of the 28th Euromicro Conference*, pp 183-188.
- Yang, X. & Latecki, L.J. (2010) Weakly Supervised Shape Based Object Detection with Particle Filter. *European Conference on Computer Vision (ECCV)*.

Other relevant papers

Xingwei Yang, Hairong Liu, and Longin Jan Latecki, Contour-Based Object Detection as Dominant Set Computation. *Pattern Recognition (PR)*, to appear.

Tianyang Ma and Longin Jan Latecki. Maximum Weight Cliques with Mutex Constraints for Video Object Segmentation. *IEEE Conf. on Computer Vision and Pattern Recognition (CVPR)*, June 2011.

Xinggong Wang, Xiang Bai, Tianyang Ma, Wenyu Liu and Longin Jan Latecki. Fan Shape Model for Object Detection. *IEEE Conf. on Computer Vision and Pattern Recognition (CVPR)*, June 2011.

Xinggong Wang, Xiang Bai, Xingwei Yang, Wenyu Liu, and Longin Jan Latecki. Maximal Cliques that Satisfy Hard Constraints with Application to Deformable Object Model Learning. *Neural Information Processing Systems Conf. (NIPS)*, Barcelona, December 2011.

Tianyang Ma and Longin Jan Latecki. From Partial Shape Matching through Local Deformation to Robust Global Shape Similarity for Object Detection. *IEEE Conf. on Computer Vision and Pattern Recognition (CVPR)*, Colorado Springs, June 2011.

Xinggong Wang, Xiang Bai, Wenyu Liu, and Longin Jan Latecki. Feature Context for Image Classification and Object Detection, *IEEE Conf. on Computer Vision and Pattern Recognition (CVPR)*, Colorado Springs, June 2011.

Wei Shen, Xiang Bai, Rong Hu, Hongyuan Wang, and Longin Jan Latecki. Skeleton Growing and Pruning with Bending Potential Ratio. *Pattern Recognition (PR)*, 44, pp. 196-209, 2011.

Hairong Liu, Longin Jan Latecki, Shuicheng Yan. Robust Clustering as Ensemble of Affinity Relations, *Neural Information Processing Systems Conf. (NIPS)*, Vancouver, December 2010.

Xingwei Yang and Longin Jan Latecki. Weakly Supervised Shape Based Object Detection with Particle Filter. *European Conference on Computer Vision (ECCV)*, September 2010.

Tianyang Ma, Xingwei Yang, and Longin Jan Latecki. Boosting Chamfer Matching by Learning Chamfer Distance Normalization. *European Conference on Computer Vision (ECCV)*, September 2010.

Haibin Ling, Xingwei Yang, and Longin Jan Latecki. Balancing Deformability and Discriminability for Shape Matching. *European Conference on Computer Vision (ECCV)*, September 2010.

Hairong Liu, Wenyu Liu, Longin Jan Latecki. Convex Shape Decomposition. *IEEE Conf. on Computer Vision and Pattern Recognition (CVPR)*, San Francisco, June 2010.

ChengEn Lu, Nagesh Adluru, Haibin Ling, Guangxi Zhu, Longin Jan Latecki. Contour Based Object Detection Using Part-Bundles. *Computer Vision and Image Understanding (CVIU)*, Vol. 114, No. 7, pp. 827-834, July 2010.

- Longin Jan Latecki, Marc Sobel, and Rolf Lakaemper. Piecewise Linear Models with Guaranteed Closeness to the Data. *IEEE Trans. Pattern Analysis and Machine Intelligence (PAMI)*, Vol. 31, No. 8, pp. 1525-1531, 2009.
- Nagesh Adluru and Longin Jan Latecki. Contour Grouping Based on Contour-Skeleton Duality. *International Journal of Computer Vision (IJCV)* 83, pp. 12-29, 2009.
- ChengEn Lu, Longin Jan Latecki, Nagesh Adluru, Xingwei Yang, and Haibin Ling. Shape Guided Contour Grouping with Particle Filters. *12th IEEE Int. Conf. on Computer Vision (ICCV)*, Kyoto, Japan, Sep./Oct. 2009.
- Xiang Bai, Xinggong Wang, Longin Jan Latecki, Wenyu Liu, and Zhuowen Tu. Active Skeleton for Non-rigid Object Detection. *12th IEEE Int. Conf. on Computer Vision (ICCV)*, Kyoto, Japan, Sep./Oct. 2009.
- X. Bai, X. Yang, L. J. Latecki, Z. Tu, and W. Liu. Shape Band: A Deformable Object Detection Approach. *IEEE Conf. on Computer Vision and Pattern Recognition (CVPR)*, June 2009.